nature chemistry

SUPPLEMENTARY INFORMATION

DOI: 10.1038/NCHEM.2618

Multistep nucleation of nanocrystals in aqueous solution

N. Duane Loh[1, 2], Soumyo Sen[3], Michel Bosman[4, 5], Shu Fen Tan[6], Jun Zhong[1, 2]

Christian A. Nijhuis[6, 7]†, Petr Král[3, 8]†, Paul Matsudaira[2, 9], Utkur Mirsaidov[1, 2, 7, 10]†

1. Department of Physics, National University of Singapore, Singapore 117551, Singapore.
2. Centre for BioImaging Sciences, Department of Biological Sciences, National University of Singapore, Singapore 117543, Singapore.
3. Department of Chemistry, University of Illinois at Chicago, Chicago, Illinois 60607, USA.
4. Institute of Materials Research and Engineering, A*STAR (Agency for Science, Technology and Research), Singapore 138634, Singapore.
5. Department of Materials Science and Engineering, National University of Singapore, Singapore 117575, Singapore.
6. Department of Chemistry, National University of Singapore, 117543, Singapore.
7. Centre for Advanced 2D Materials and Graphene Research Centre, National University of Singapore, Singapore 117546, Singapore.
8. Department of Physics and Biopharmaceutical Sciences, University of Illinois at Chicago, Chicago, Illinois 60607, USA.
9. MechanoBiology Institute, National University of Singapore, Singapore 117576, Singapore.
10. NanoCore, National University of Singapore, Singapore 117576, Singapore.

Table of contents:

Supplementary Movie Captions:

Supplementary Movie 1: TEM movie of particle nucleation at electron dose rate of 3300 e $Å^{-2}$ s^{-1}.
Supplementary Movie S2: TEM movie of particle nucleation at electron dose rate of 830e $Å^{-2}$ s^{-1}
Supplementary Movie S3: TEM movie of particle nucleation at electron dose rate of 1650 e $Å^{-2}$ s^{-1}

Supplementary Section 1. Materials and Methods:

Materials: The liquid cell, micro-fabricated from 200 μm-thick silicon wafers, has two 14 nm thick electron-translucent silicon nitride (SiN_x) membrane windows with lateral dimensions of ~10×50 μm. These membrane windows are separated with a 200 nm spacer.[1] The SiN_x membranes are plasma cleaned before liquid cell assembly and also right before loading the solution to render the membrane surfaces hydrophilic. We loaded approximately 400 nL of aqueous precursor solution containing 1 mM of $HAuCl_4$ (Sigma Aldrich: Cat#54349) into the liquid cell and sealed the loading pockets with a gasket. Next, the liquid cell is inserted into the TEM using a specimen holder. Inside the TEM, the electron beam passes through the top and the bottom SiN_x membranes, and the aqueous solution layer sandwiched between these membranes.

TEM Imaging: Two different TEMs were used for *in situ* imaging, JEOL 2010FEG for TEM imaging and FEI Titan for STEM imaging, both with 200 kV electrons at doses ranging from 800 to 8000 e $Å^{-2}$ s^{-1}. We recorded movies at frame rate of 10 Hz and at a magnification of 250,000× to 400,000× using an Orius SC200 CCD camera (Gatan, Inc., USA).[2]

Supplementary Section 2. Electron dose estimation and radiolysis.

Since the number of water molecules per unit volume vastly exceeds that of gold atoms before irradiation, we presume that the radiation dose due to the fast electrons is effectively absorbed by the water. This dose on liquid water can be estimated by the Bethe-Bloch formula for stopping power,[3] valid for electron energies well-above 10 keV, and is captured by the following formula for the average energy loss per electron per unit of specimen penetration:

$$\left\langle \frac{dE}{dx} \right\rangle = -\rho_w \frac{0.153536}{\beta^2} \frac{Z}{A} B(T)\,. \quad \text{(Supp. Eq. 1)}$$

Here, $B(T) = \log\left(\frac{\tau^2(\tau+2)}{2}\right) + \frac{1+\frac{\tau^2}{8}-\log(2)(2\tau+1)}{(\tau+2)^2} - 2\log(I/m_0c^2) - \delta$, T is the average kinetic energy of electrons (we used 200 keV electrons), $\tau = T/m_0c^2$ is the relative kinetic energy, m_0 is the rest mass of electrons, $\beta = \frac{v}{c} = \sqrt{1-1/(1+\tau)^2}$ is the average relative speed of electrons with respect to the speed of light, $I = 75$ eV [3] is the mean excitation energy of water, $\rho_W = 1$ g cm^{-3} is the assumed density of water, and δ the density effect correction is ignored here. From these equations, we find that $\left\langle \frac{dE}{dx} \right\rangle \approx -0.0208$ eV $Å^{-1}$.

Hence, the radiation dose rate on a patch of liquid water of a cross sectional area ΔA and thickness Δx along the electron propagagtion direction from the incident electron flux of $j_e = 10^3$ $Å^{-2}$ s^{-1} is,

$$\Phi = \frac{-\left\langle \frac{dE}{dx} \right\rangle \Delta x\, J_e\, \Delta A}{\rho_w\, \Delta x\, \Delta A} = 4.5 \times 10^9 \text{ Gy s}^{-1}. \quad \text{(Supp. Eq. 2)}$$

Such a high dose rate produces large quantities of radiolysis products. Supp. Table 1 summarizes key properties of these products.

	G-value (per 100eV)	$\tau_{1/2}$ (10^{-6} s)	V_{red} (V)
Solvated electron, e_{aq}^-	2.6 [4]	50 [5]	-2.1 [4]
Hydroxyl free radical, OH·	2.7 [4]	10 [6]	+1.7 [4]
Hydrogen free radical, H·	0.6 [4]		-2.1 [4]
Molecular Hydrogen, H_2	0.4 [5]		

Supp. Table 1: Summary of key parameters of radiolytic chemical species expected in the liquid cell. Here, V_{red} and $\tau_{1/2}$ - reduction potential and half life time of species.

A Fricke *G*-value of one (second column of Supp. Table 1) corresponds to radiolytic production of 1 particle for every 100 eV of absorbed radiation. Two dominant products are produced here: the reducing solvated electrons, e_{aq}^-, and the oxidizing OH• free radical. The next most abundant products are H_2 and H• radical, which we ignore due to their low G-values and high diffusivities.

These Linear-Energy-Transfer (LET) G-values are applicable only if the cluster of radiolysis by-products, termed spurs, produced by high-energy electrons do not spatially overlap. Here we adopt the approach of Grogan *et al.*[5] to show that the spurs that we have created do not overlap, even at our highest flux of 3300 e Å^{-2} s^{-1}. The average variance in distribution of radiolysis products in a spur is $\sigma_{spur} \sim 1.2$ nm,[7] and we assume that spurs are well-separated if their average distance is greater than $5\sigma_{spur}$. Then the average number of spurs produced by electrons per spur's lifetime is $n = h_{liq}It/\lambda e$, where I is the electron current, t is the lifetime of the spur (~1 μs), and λ is the mean free path of the electron in water (~50 nm for a 200 keV electron). When we evenly distribute these n spurs along the cylindrically irradiated volume of radius a, $V_{rad} = h_{liq}(\pi a^2)$, and assume that the average volume where only one spur occurred occupies a spherical volume of $V_d = 4\pi(d_{spur}/2)^3/3$. Equating these $nV_d = V_{rad}$ gives us $d_{spur} \sim 10$ nm $> 8\ \sigma_{spur}$. Hence, the LET G-values are applicable to our experiment.

Given the above imaging conditions of our liquid cell (Supp. Fig. 1), consider a fraction of the irradiated volume within a $\lambda_{DL} = 10$ nm liquid film in the liquid cell's membrane $V_{AuDL} = \lambda_{DL}(\pi r_{Au}^2) \approx 800$ Å^3 (the average Au-Au separation in gold solid is $r_{Au} = 1.6$ Å) produces e_{aq}^- at a rate of $R_e \approx 584$ s^{-1}. Assuming that the solvated electrons have a half-life of ~50 microseconds,[8] steady state occurs when radiolytic production rate equals decay rate,

$$\frac{dN_e}{dt} = -\frac{\log_2 N_e}{\tau_{1/2}} + R_e = 0. \qquad \text{(Supp. Eq. 3)}$$

At steady state this irradiated volume V_{AuDL} should contribute ~0.04 (87 mM) solvated electrons. For regions of homogeneous liquid density that receive uniform electron current, the average steady-state solvated electron concentrations should be nearly identical between adjacent V_{AuDL} volumes. For simplicity, we ignored Fick's diffusion in Supp. Eq. 3 in the viewing regions, where concentration gradients of radiolysis-products are small due to uniform electron illumination. Furthermore, we also expect the diffusion coefficients in the double layer to be highly damped. However, diffusion should be enhanced closer to the edges of the electron beam where the electron current falls drastically. This diffusion explains why radiolytic reduction and nucleation of gold occur even outside the electron-irradiated field of view.

Hydroxyl free radicals are known to have a strong oxidizing potential of ~2.7 V (Supp. Table 1) and can increase the oxidation state of gold. However, because of its shorter half-life than that of an electron (Supp. Table 1), the steady-state number of hydroxyl free radicals is 0.008 (18 mM) in the same volume V_{AuDL}, which is five times lower than that of solvated electrons.

Overall, we observed that gold nucleation in the thin liquid film is accelerated by electron beam irradiation (Supp. Fig. 2). This is further confirmed by Gachard *et al.*,[9] who showed that gold ions in a 1 mM $KAuCl_4$ aqueous solution reduce completely beyond a 10 kGy dose from a pulsed high-energy electron source. Comparatively, the illuminated volume of our 1 mM $HAuCl_4$ solution is exposed to a dose that is 10^6 larger within about one second of exposure (or 10^7 higher for movies that span 10 s). However, while the majority of $[Au^{III}Cl_4]^-$ ions present in solution should reduce to zero-valent gold in the illuminated volume, we cannot preclude some oxidation back to $[Au^{I}Cl_2]^-$ ions due to the considerable concentration of OH• radicals.

In summary, a characteristic cylindrical liquid column $V_{AuDL} = \lambda_{DL}(\pi r_{Au}^2) \approx 800$ Å^3 (the average Au-Au separation in gold solid is $r_{Au} = 1.6$ Å) contains an average ~0.5 gold atoms at concentration $c_i^{(Au)}$ of ~ 1 M, ~27 water molecules in bulk water, ~42 atoms in liquid gold (17.3 g cm^{-3}) and a meager 8×10^{-13} atoms for a saturated gold solution. At a current of 1000 e Å^{-2} s^{-1} the TEM should produce an average steady population of at most ~0.04 solvated electrons within a neat water column of volume V_{AuDL}.

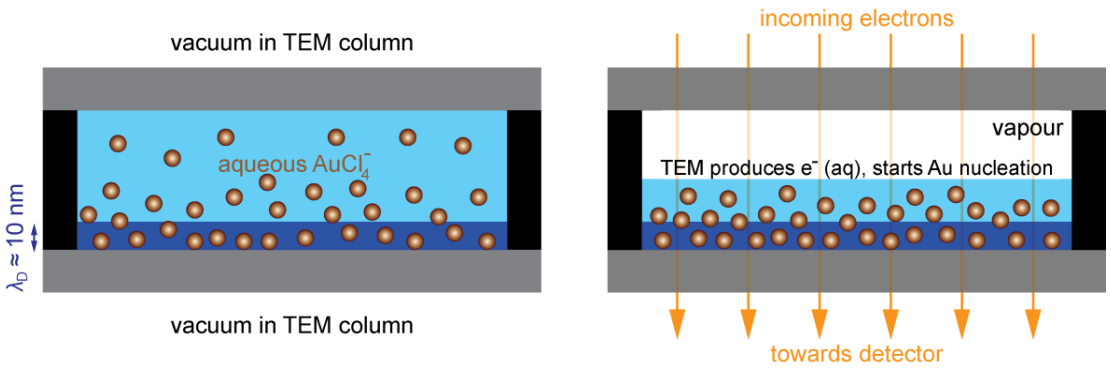

Supp. Fig. 1: Schematic of liquid cell electron microscopy. Schematic of the liquid cell used in the Transmission Electron Microscope (TEM). High local concentrations of $Au(III)Cl_4^-$ (orange spheres) near the cell's silicon nitride membranes are chemically reduced to Au^0 by solvated electrons, $e^-(aq)$, produced by the electron beam, resulting in liquid-phase demixing. The Debye layer thickness (dark blue region), λ_{DL}, is estimated to be around 10 nm.

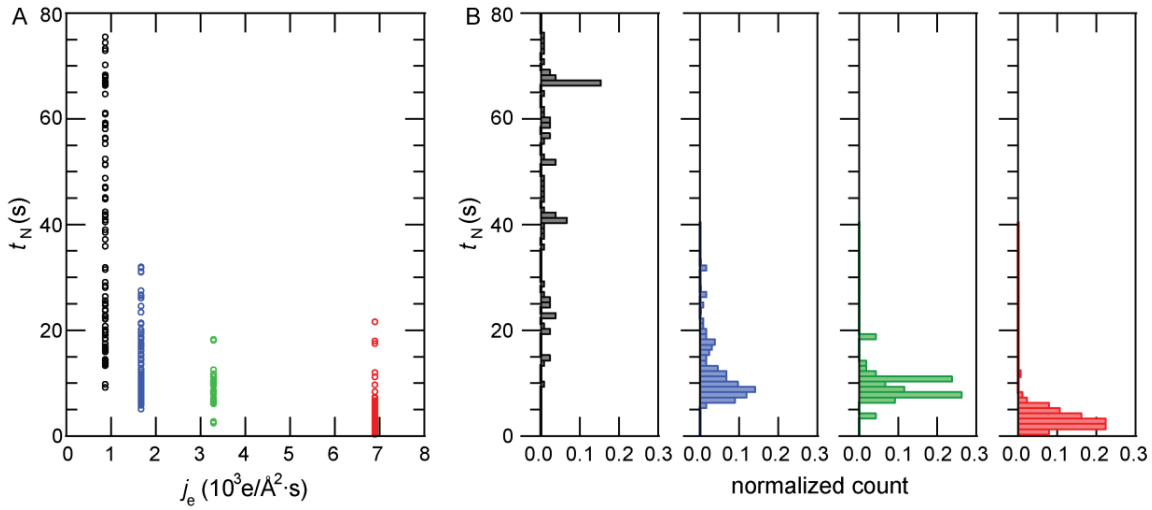

Supp. Fig. 2: Particle formation times versus electron dose rate. (**A**) Time it takes for a particle to be first detected, t_N, versus electron flux, j_e. (**B**) Histogram associated with the particle formation when imaged at different electron dose rates. t_N is the time to the observation of nuclei.

The fact that the number of nanoclusters do not increase drastically with high electron dose rates (6000 e Å^{-2} s^{-1} example not shown here) suggests that the mechanism for nucleation in our liquid cell could either be diffusion-limited – fresh Au does not enter the field of view quickly enough – or that electrophoretic expulsion of Au occurs at high electron currents.

Supplementary Section 3. Electron-beam induced heating of solution.

We turn our attention to potential thermal heating of the liquid cell due to the TEM beam. Note that the high surface area-to-volume ratio of the thin liquid ensures efficient heat conduction from the irradiated liquid to the liquid cell's silicon nitride membrane. Specifically, retracing the arguments in the Supplementary Materials of Mirsaidov *et al.*,[10] we find that the temperature of the silicon nitride membrane is elevated by 1 K with each additional ~80 e Å^{-2} s^{-1} of electron dose rate for an illuminated area of 5 µm in radius. For the three electron fluxes in the main text (830, 1650, 3300 e Å^{-2} s^{-1}) and illuminated area of 500 nm in radius, this translates to a maximum temperature rise of ~ 1.3 K, 2.6 K and 5.1 K. These are less than 0.4 % of gold's bulk melting temperature at 1 atm of 1337 K, and do not cause water to boil. Such low-level beam-induced heating is consistent with observations of nanoparticle nucleation even at electron fluxes up to 6900 e Å^{-2} s^{-1} (Supp. Fig. 2), where only a modest 10 K heating is expected. The derivation of this calculation is detailed below.

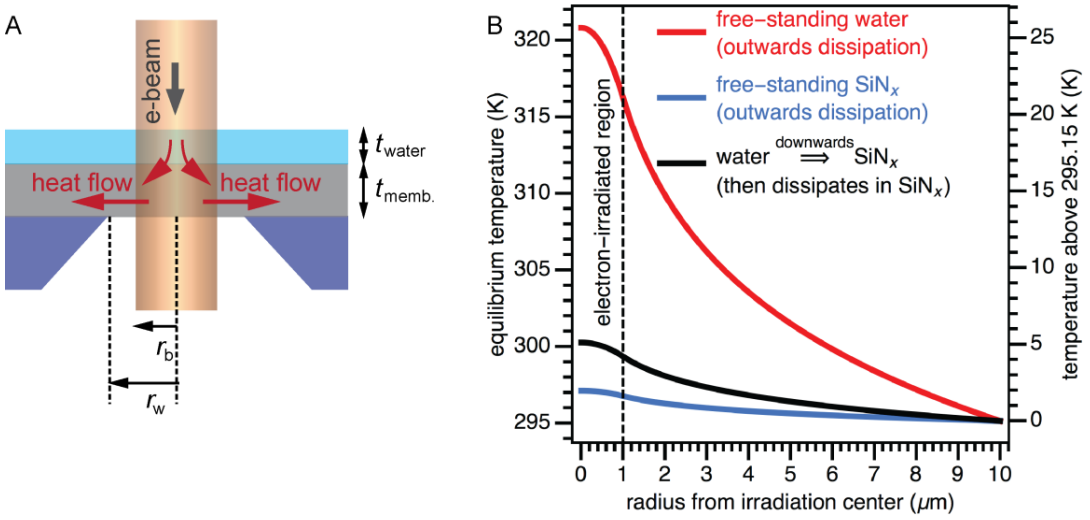

Supp. Fig. 3. (**A**) Schematic of water film on SiN_x membrane under electron-irradiation. Electron beam transfers energy both to the water film and free standing SiN_x membrane. Absorbed energy of water and membranes dissipates laterally into the membrane to thick *Si* frame of the chip, which is in direct contact with the specimen holder. (**B**) Estimated temperature increase as a function of radius from center of electron-irradiation, assuming an electron flux of 3300 e Å^{-2} s^{-1}. Three cases are considered here: (**red**) a free-standing 30-nm thick film of water where heat from electron-irradiation is dissipated radially outwards; (**blue**) a free-standing 20-nm thick silicon nitride membrane where heat from electron-irradiation is dissipated radially outwards; (**black**) the same water film in thermal contact with the nitride membrane with downwards thermal dissipation (water to membrane), followed by outwards dissipation within the membrane. The large contact surface between water and membrane, coupled with silicon nitride's higher thermal conductivity compared to water, makes the membrane an effective conduit for thermal dissipation.

First, we list the parameters of our liquid cell and TEM imaging conditions. We approximate a cylindrical thermal heat sink held at $T_0 = 295.15$ K, at a radius of $r_w \approx 10$ µm from the center of electron irradiation in the silicon nitride membrane. The electron beam is assumed to have an uniform electron flux and a radius of $r_b \approx 2$ µm. The membrane is $t_m \approx 20$ nm thick, has a thermal conductivity of $\kappa_m \approx$ 4.9 W/(m·K) ,[11] and suffers joule heating of $(dE/dx)_m = 2.09\times10^{-11}$ J/m (Supp. Eq. 1). The liquid film

is assumed to have thermal properties comparable to water, with a thermal conductivity of $\kappa_w \approx 0.6$ W/(m·K), and a joule heating of $(dE/dx)_w = 3.33\times10^{-11}$ J/m.

We expect that the thermal current $(dQ/dt)_w$ in the liquid film generated by electron irradiation is first dissipated down into the silicon nitride membrane, then dissipated radially outwards to the liquid cell's heat sink (Supp. Fig. 3A). We support this expectation by two arguments.

First, compared to thermal transport radially outwards to non-irradiated liquid in the thin film, thermal transfer from irradiated water to membrane is favored by the much larger heat transport area: the area of an irradiated disk-like surface is 17 times higher than for a cylindrical surface in the liquid film. The ratio of radial (ΔT_{w_rad}) versus vertical (ΔT_{w_vert}) temperature difference that is needed to transport joule heating from irradiation is $\Delta T_{w\_rad}/\Delta T_{w\_vert} \approx 555$. Therefore, a much smaller temperature gradient is needed to dissipate heat vertically into the silicon nitride membrane than radially outwards to the surrounding liquid. Second, the thermal conductivity of the silicon nitride is eight times higher than that of water. This naturally makes silicon nitride the path of least thermal resistance towards the heat sink at $r = r_w$.

Now that we have justified the two-step thermal dissipation model in Supp. Fig. 3A, let's consider the vertical temperature differences expected in this model. We can obtain an upper bound on the liquid film's temperature by ignoring radial thermal dissipation into surrounding liquid. In this case, a small temperature difference of

$$\Delta T_{w\_vert} \approx j_e\,(dE/dx)_w\,t_w^2 / k_w \approx 0.017 \text{ K}, \text{ (Supp. Eq. 4)}$$

between the top and bottom surfaces of the t_w-thick liquid film is needed to move the electron-induced thermal load into the silicon nitride membrane. Similarly, the silicon nitride membrane also needs a vertical temperature gradient to distribute this heat vertically so that it can in turn be dissipated efficiently towards the heat sink (Supp. Fig. 3A). This temperature difference in silicon nitride is a meagre

$$\Delta T_{m\_vert} \approx j_e\,(dE/dx)_w\,t_w\,t_m / k_m \approx 0.0013 \text{ K}. \text{ (Supp. Eq. 5)}$$

The vertical temperature differences in Supp. Eqs. 4-5 needed for thermal transport are essentially negligible and we can assume a two-dimensional heat diffusion in the silicon nitride membrane instead that bears the full load of dissipating the joule heating of both the liquid film and silicon nitride membrane. As a final simplification, we seek only a radially-dependent temperature distribution $T(r)$ owing to the cylindrical-symmetry expected in the electron beam, silicon nitride membrane and liquid film.

Following the assumptions above, the temperature increase in silicon nitride at steady state can be computed using the two-dimensional heat conduction equation in cylindrical coordinates (Supp. Fig. 3A):

$$\frac{dT(r)}{dt} \approx \kappa_m \left(\frac{d^2T(r)}{dr^2} + \frac{1}{r}\frac{dT(r)}{dr}\right) + J = 0, \text{ (Supp. Eq. 6)}$$

where $T(r)$ is temperature as a function of r the distance to the center of heat source, J is the thermal current density from joule heating in both water and silicon nitride membrane. Outside the illumination region, $r > r_b$, we know that $J = 0$, so the heat sink imposes a boundary condition of $T(r_w) = T_0$, and the energy conservation requires a heat flux of

$$\frac{dT(r)}{dr} = \frac{1}{2\pi r_b t_m \kappa_m}\left(\frac{dQ}{dt}\right)_{w+m}$$

Heat flows from the electron beam irradiated area of radius r_b to the heat sink at the edge of membrane window (Si frame of the chip at $r = r_w \approx 10$ μm – window radius) where we assume the heat sink

temperature to be at ambient temperature, $T = T_0$. Solving Supp. Eq. 6 for the temperature profile outside the electron-irradiated region gives:

$$T(r) = T_0 + j_e {r_b}^2 \frac{(\mathrm{d}E/\mathrm{d}x)_m + (\mathrm{d}E/\mathrm{d}x)_w}{2\kappa_\mathrm{m}} \log(r_\mathrm{w}/r). \quad \text{(Supp. Eq. 7)}$$

The solution to Supp. Eq. 6 inside the electron-irradiated zone ($r < r_\mathrm{b}$) yields a temperature profile of

$$T(r) = T_0 + j_e \frac{(\mathrm{d}E/\mathrm{d}x)_m + (\mathrm{d}E/\mathrm{d}x)_w}{2\kappa_\mathrm{m}} \left({r_b}^2 \log(r_\mathrm{w}/r_\mathrm{b}) + 0.5({r_\mathrm{b}}^2 - r^2)\right), \quad \text{(Supp. Eq. 8)}$$

where we applied the condition that the temperatures in Supp. Eq. 7 and Supp. Eq. 8 between the irradiated and non-irradiated areas have to match at $r = r_\mathrm{b}$. These relations in Supp. Eq. 7 and Supp. Eq. 8 are computed in Supp. Fig. 3B, for the electron flux of 3300 e Å^{-2} s^{-1}. Because $T(r)$ scales linearly with electron flux j_e, the temperature within the liquid cell should double with a doubled electron flux.

Supplementary Section 4. Radiolysis induced reactions in solution.

The reduction of chloroauric acid, $HAuCl_4$, by radiolysis is well studied at lower ionizing doses.[9] For completeness we list some of the known redox pathways from earlier studies. With their very negative standard reduction potential ($E(H_2O/e_{aq})$ ~ 2.87 V), solvated electrons very quickly reduce Au(III) to Au(II):

$$[Au^{III}Cl_4]^- + e_{aq}^- \rightarrow [Au^{II}Cl_4]^{2-} \ . \qquad \text{(Supp. Eq. 9)}$$

According to Gachard *et al.*[9], the reduction potential of $E(Au^{III}Cl_4^-/Au^{II}Cl_4^{2-})$ ~1. Au(II) then very rapidly disproportionates to Au(I) and Au(III), with a rate constant of 5×10^8 L mol^{-1} s^{-1}:

$$2[Au^{II}Cl_4]^{2-} \rightarrow [Au^{III}Cl_4]^- + [Au^{I}Cl_2]^- + 2\ Cl^- \ . \text{ (Supp. Eq. 10)}$$

This reduction continues from Au(I) to Au(0) again by the action of solvated electrons:

$$[Au^{I}Cl_2]^- + e_{aq}^- \rightarrow [Au^{0}Cl_2]^{2-} \ . \text{ (Supp. Eq. 11)}$$

However, the hydroxyl free radical has a fairly positive standard reduction potential (+2.7 V and +1.7 V in acidic and neutral solutions respectively (Supp. Table 1)), and given their considerable supply within the liquid cell, they may easily oxidize Au(0) and Au(I) back into the higher oxidation states. In fact, earlier demonstrations with radiolysis-induced nucleation showed that the addition of scavengers of OH radicals (e.g. 2-propanol or poly-vinyl alcohol) can accelerate reduction and hence nucleation. Such scavengers were absent in our reported experiments.[9]

It has been further hypothesized that these radiolytically formed gold ions associate to form dimers and aggregate into clusters of steadily increasing nuclearity.[9] The following captures the expected sequence of events:

$$\begin{gathered} Au^{0}Cl_2^{2-} + Au^{I}Cl_2^- \rightarrow (Au_2^+)_{Cl^-} \\ 2(Au_2^+)_{Cl^-} \rightarrow (Au_4^{2+})_{Cl^-} \\ (Au_q^{z+})_{Cl^-} + (Au_p^{y+})_{Cl^-} \rightarrow (Au_n^{x+})_{Cl^-} \ , \text{ (Supp. Eq. 12)} \end{gathered}$$

where (q, p, n) represent the nuclearities of the gold clusters. Similar behavior has been observed for the radiation-induced synthesis of metallic clusters.[12] The study Gachard *et al.*,[9] however, found

evidence that the earliest clusters that form are unlikely to be zero-valent oligomers due to their missing plasmon signatures.

Another recent experiment with radiolysis-induced nucleation also supports the cluster formation hypothesis.[13] However, this study further indicates that much of the gold within the precursors to nucleation are notably dissimilar to bulk crystalline gold. These were inferred from dominant signatures of Au-Cl bonds in these precursors, as well as dilated Au-Au bond distances compared to crystalline gold. Overall, these studies strongly suggest that radiolysis-induced precursors to gold nucleation do not resemble those of bulk gold crystals, and that the classical notion of crystalline nuclei may not apply.

Supplementary Section 5. Estimating the amount of gold that precedes the formation of gold nanoparticles.

To estimate the gold concentration from dark field Scanning TEM (STEM) image (Supp. Fig. 4A) we use a simplified schematic shown in Supp. Fig. 4B. Dark field STEM images were obtained with an FEI Titan TEM having an ADF detector collection semiangle between 50 and 200 mrad. The electron beam was focused to an electron probe with a diameter less than 0.4 nm, which rapidly raster-scanned an area of 66×66 nm. For a dark field imaging the scattering from gold is the dominant factor, as the counts in ADF images are approximately proportional to the average local atomic number. The ratio of the elastically scattered electron to the total number of electrons from composite specimen layers (1, 2, …) arriving at the ADF detector can be expressed as:[14]

$$N/N_0 = 1 - \exp\left[-\left(L_1/\lambda_1 + L_2/\lambda_2 + \cdots\right)\right]. \quad \text{(Supp. Eq. 13)}$$

where L and λ are specimen thickness and mean free path for elastic scattering. We use a first order approximation from a Taylor expansion for the structure depicted in Supp. Fig. 4B:

$$N_a \cong N_0\left(L_{np(a)}/\lambda_{Au} + L_{Au\ film}/\lambda_{Au} + L_{SiN}/\lambda_{SiN} + L_{water}/\lambda_{water}\right) = N_{np(a)} + N_{Au\ film} + N_{SiN} + N_{water}\ .$$ (Supp. Eq. 14)

The total number of scattered electrons reduces to the sum of electrons scattered from each structure layer shown in Supp. Fig. 4B. The number of elastically scattered electrons from a nanoparticle a, $np(a)$, with a diameter of $L_{np(a)}$ = 8 nm can simply be written as:

$$N_{np(a)} \cong \frac{N_0 L_{np(a)}}{\lambda_{Au}}. \quad \text{(Supp. Eq. 15)}$$

Therefore, we can express the thickness of the hypothetical gold film associated with our gold solution as ($N_{Au\ film}$ = 4000 and $N_{np(a)}$ = 24000 from Supp. Fig. 4C):

$$L_{Au\ film} \cong \frac{\lambda_{Au} N_{Au\ film}}{N_0} \cong \frac{N_{Au\ film} L_{np(a)}}{N_{np(a)}} = \frac{4000\times 8\ nm}{24000} = 1.3\ \text{nm}. \quad \text{(Supp. Eq. 16)}$$

We can easily check that this scaling argument is valid by estimating the size of the nanoparticle b with a measured diameter of 5 nm, for which using Supp. Eq. 16 we get 4.9 nm. Therefore, scattering coming from the film of gold solution is equivalent to the scattering from a $L_{\text{Au film}}$ = 1.7 nm thick gold layer.

In order to estimate the gold concentration prior to nucleation we need first to estimate the thickness of the water film on the SiN_x membrane using similar arguments. The number of scattered electrons for SiN_x:

$$N_{SiN} \cong \frac{N_0 L_{SiN}}{\lambda_{SiN}}, \quad \text{(Supp. Eq. 17)}$$

where L_{SiN} is the thickness of the SiN_x membranes (L_{SiN}~2×15 nm = 30 nm). The mean free path for elastic scattering is defined as:

$$\lambda = \frac{A}{\rho \sigma N_A}, \quad \text{(Supp. Eq. 18)}$$

where A - mass number, ρ - density, N_A- Avogadro number, σ- scattering cross-section. We used the following cross-sections: $\sigma_{water} = 0.11\sigma_H + 0.89\sigma_O = 5\times10^{-19}$ cm^2, $\sigma_{SiN} = 0.67\sigma_{Si} + 0.33\sigma_N = 1.4\times10^{-18}$ cm^2, and $\sigma_{Au} = 14.4\times10^{-18}$ cm^2.[15]

Now we can combine Supp. Eq. 15, 17 and 18 to obtain:

$$\frac{N_{SiN}}{N_{np(a)}} \cong \frac{\sigma_{SiN}}{\sigma_{Au}} \frac{A_{Au}\rho_{SiN}}{A_{SiN}\rho_{Au}} \frac{N_{np(a)}L_{SiN}}{L_{np(a)}} \approx \frac{2120}{23000}. \quad \text{(Supp. Eq. 19)}$$

Then the ratio of scattered electrons from the water film to the electrons scattered from gold film will be (Supp. Fig. 4B): $^{(4000-2120)}/_{24000} = {}^{1880}/_{24000}$, and we arrive at a water film thickness of:

$$L_{water} \cong \frac{N_{water}}{N_{np(a)}} \frac{\sigma_{Au}}{\sigma_{water}} \frac{A_{water}\rho_{Au}}{A_{Au}\rho_{water}} L_{np(a)} \approx 32 \text{ nm}. \quad \text{(Supp. Eq. 20)}$$

With the film of gold solution composed of L_{water}=32 nm thick water and L_{Au}=1.3 nm gold, we can easily arrive at the final concentration of the pre-nucleation solution:

$$[Au] = \frac{\rho_{Au} L_{Au}}{A_{Au} L_{water}} \approx 4 \text{ M},$$

where ρ_{Au} = 19300 g/L and A_{Au} = 197. This estimated number suggests that the local concentration at the particle formation is about 3 orders of magnitude higher than 1 mM stock solution used in our experiments. It is important to note that the water film thickness is only a rough estimate. However, the upper bound for the film thickness would be ~200 nm, since we are using a ~200 nm thick spacer between two membranes. Even for this case we would get ~0.6 M.

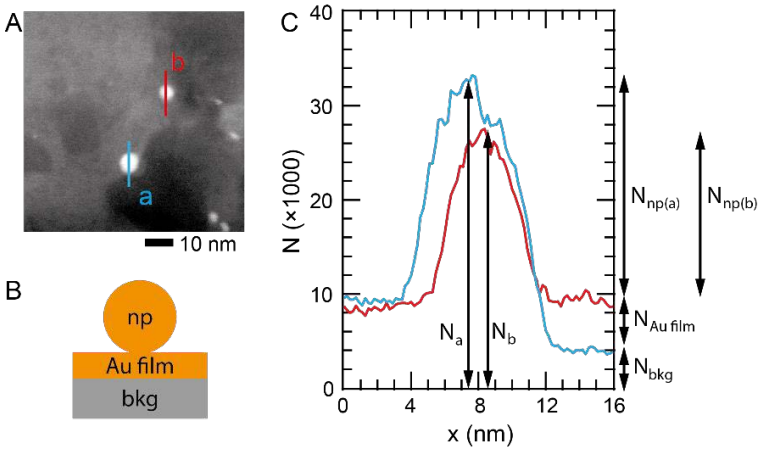

Supp. Fig. 4: STEM images of nanoparticles and surrounding gold solution during nucleation. (**A**) STEM annular dark field image showing gold nanoparticles ***a*** and ***b*** and surrounding gold solution. (**B**) A simplified depiction of the path of scattered electrons. Background (bkg) includes SiN_x film water film. (**C**) ADF detector counts obtained from a line profile over nanoparticles ***a*** and ***b***.

Supplementary Section 6. Imaging with Annular-Dark-Field Scanning Transmission Electron Microscopy.

In Annular-Dark-Field Scanning Transmission Electron Microscopy (ADF-STEM) a specimen is rastered with a scanning electron probe and the number of electrons scattered away from the direct beam are measured by an annular detector (Supp. Fig. 5). The electron probe's typical beam current is ~0.5 nA (3×10^9 electrons/s), rastering a 1024×1024 field of view at 10 Hz. Therefore, each square pixel (with area 1.8 Å^2) is visited ten times per second by a probe that dwells for 9.5×10^{-8} s per visit. On average, the specimen receives ~ 1700 e Å^{-2} s^{-1}, although the peak electron flux is approximately 2×10^{10} e Å^{-2} s^{-1}.

From Supp. Fig. 5 we see that despite the high peak electron flux gold-rich spinodal structures measuring several nanometers in its smallest dimension form out of solution, from which gold nanoclusters eventually appear. This sequence of steps is similar to the multi-step nucleation observed with TEM at 1650 e Å^{-2} s^{-1} (Figure 2 in main text).

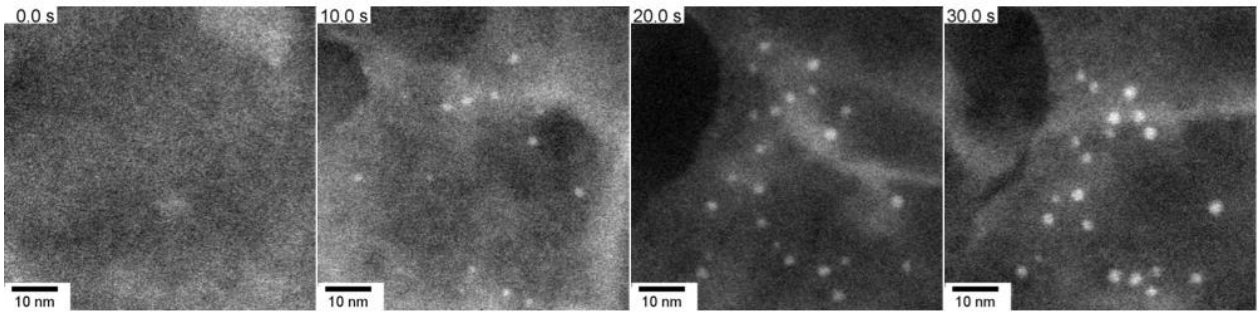

Supp. Fig. 5: Imaging multi-step gold nucleation in solution using Annular Dark-field Scanning Transmission Electron Microscopy (ADF-STEM). ADF-STEM measures the number of incident electrons that suffer large changes in momentum when a scanning electron probe interacts with the specimen. Because high-Z atoms such as gold scatter electrons more effectively than lower-Z atoms (e.g. oxygen, hydrogen, silicon, nitrogen, chlorine atoms), ADF-STEM provides very good contrast between gold-rich (light) and gold-poor (dark) regions of the solution.

Supplementary Section 7. The effect of the double layer in the liquid cell.

The number of gold atoms expected in the initial 1 mM $HAuCl_4$ solution is fairly low: ~ 5-10 atoms per 20×20 nm field of view, assuming that the solution layer in the liquid cell was 20-40 nm thick. In contrast, the number of gold atoms in a 2 nm-diameter spherical gold cluster is

$$N_{\mathrm{Au(crys)}} = N_A \rho_{\mathrm{Au}} V / A_{\mathrm{Au}} \sim 250\,, \qquad \text{(Supp. Eq. 21)}$$

where $\rho_{\mathrm{Au}} = 19.3\ \mathrm{g\ cm^{-3}}$ is the density of gold nanoclusters, V is the particle volume, and $A_{\mathrm{Au}} = 197$ is the atomic number of gold. Comparison of these values shows that enrichment of gold concentration up to a factor of 50 within the field of view is needed to nucleate a 2 nm gold nanocrystal. The fact that we see several nanoclusters in a 20×20 nm^2 field of view, often larger than 2 nm in diameter (see Figure 2 in the main text, and Supp. Figs. 8, 9, 10), points to a higher degree of gold enrichment.

Comparatively, the double-layer[16] on a charged silicon nitride membrane can trap a much larger number of $AuCl_4^-$ ions. To show this, we use the Poisson-Boltzmann distribution of ions in the charged layer. The equilibrium potential due to ions in this layer $\psi(z)$ at temperature T as a function of distance from the membrane z is,

$$\psi(z) = \frac{2\,k_B T}{e}\log\left(\frac{e^{\xi_0/2}+1+(e^{\xi_0/2}-1)e^{-\kappa z}}{e^{\xi_0/2}+1-(e^{\xi_0/2}-1)e^{-\kappa z}}\right), \quad \text{(Supp. Eq. 22)}$$

where $\xi_0 = e\,\psi(0)/k_B T$, and the Debye length $\kappa = \sqrt{2\,e^2 c_{\mathrm{Bulk}}/\epsilon_0 \epsilon_R k_B T}$;[17] e is the elementary charge; $T = 293.15$ K; the vacuum permittivity ε_0, and the relative dielectric constant of water $\varepsilon_R \sim 78$; and c_{Bulk} is the concentration of ions in the bulk liquid. The Boltzmann equilibrium concentration of positive or negative ions a perpendicular distance z away from the planar membrane, $c_+(z)$ and $c_-(z)$ respectively, is simply:

$$c_\pm(z) = c_{\mathrm{Bulk}} e^{\mp\frac{q\psi(z)}{k_B T}}. \text{ (Supp. Eq. 23)}$$

These relations are captured in Supp. Fig. 6. In the main text, we noted that the concentration of gold atoms from the double layer must be at least 1 M (equivalent to $>10^4$ gold atoms in the field of view) to produce the observed number density of gold nanoclusters. Such a high concentration far exceeds the initial 1 mM bulk concentration of aqueous $HAuCl_4$. However, Supp. Fig. 6 suggests that enough $AuCl_4^-$ ions could be trapped within the lowest 10 nm portion of the double layer to supply such high local concentrations. Suppose that either plasma cleaning or knock-on effects from the TEM's high energy electrons were to raise the membrane to a substantial 300 mV potential; the resultant boundary layer can readily accommodate more than the required 10^4 gold atoms within a 54×54 nm^2 field-of-view. It is plausible for the membrane to acquire such high potentials, when considering how a 13-fold lower electron dose rate of 60 e Å^2 s^{-1} can result in relative membrane potentials of ~ 130 mV.[10]

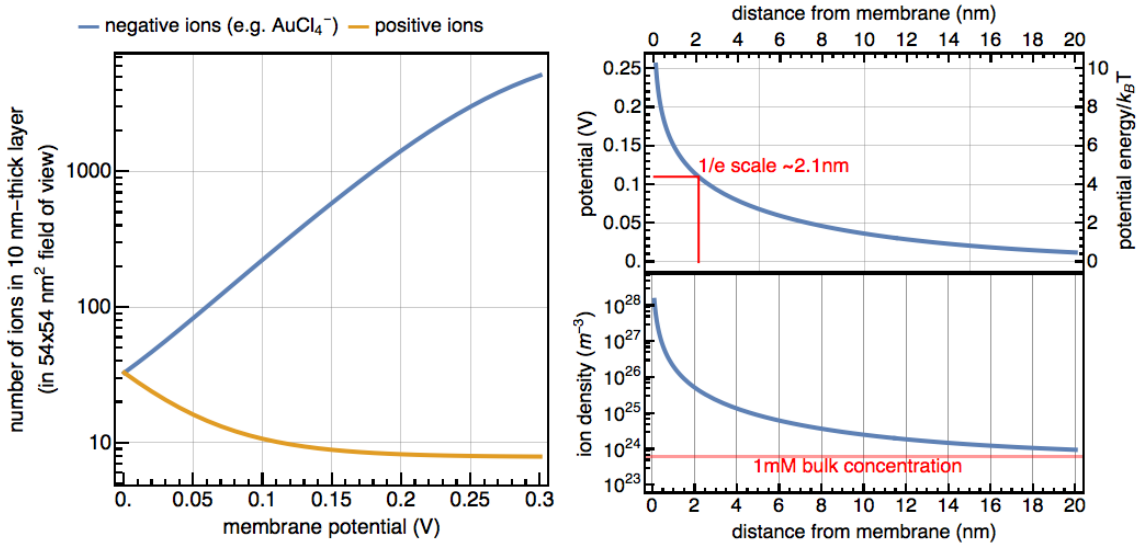

Supp. Fig. 6: Number of gold atoms in the double-layer of the silicon nitride membrane of the liquid cell, given 1 mM $HAuCl_4$(aq). Left panel: Assuming that the silicon nitride membrane is positively charged, the number of ions in a 10-nm thick and 54×54 nm^2 field-of-view double layer increases exponentially with the membrane potential. The membrane potential has to exceed 300 mV for this double layer to contain $>10^4$ gold atoms, as observed in our experiments. **Right panels**: If the membrane were at +300 mV relative to the bulk solution, we show here the equilibrium electric potential and Au-ion density in the double layer. Notice that the electrostatic energy on the average negatively charged $AuCl_4^-$ approaches $k_B T$ at a distance of 14 nm from the membrane. We implicitly assume that electrostatic forces dominated over attraction from dispersion forces (e.g. van der Waals interaction).

Further, Supp. Fig. 6 also shows that on average these negatively charged ions are in a potential well deeper than $k_B T$, until about 14 nm away from the membrane. This deep well is likely

to arrest negatively-charged gold ions (or clusters) in the double layer, which is consistent with our observations of the slow diffusion rates of gold nanoclusters in the liquid cell.

The electric potential energy of monovalent ions within λ_{DL} of the surfaces is several times k_BT, allowing us to neglect the weaker van der Waals interactions that do not scale with membrane potential.

Supplementary Section 8. Computational enhancement of cluster boundary.

Supp. Figs S7-10 and their captions describe the computational filter and algorithms used to track the nuclei formation out of solution.

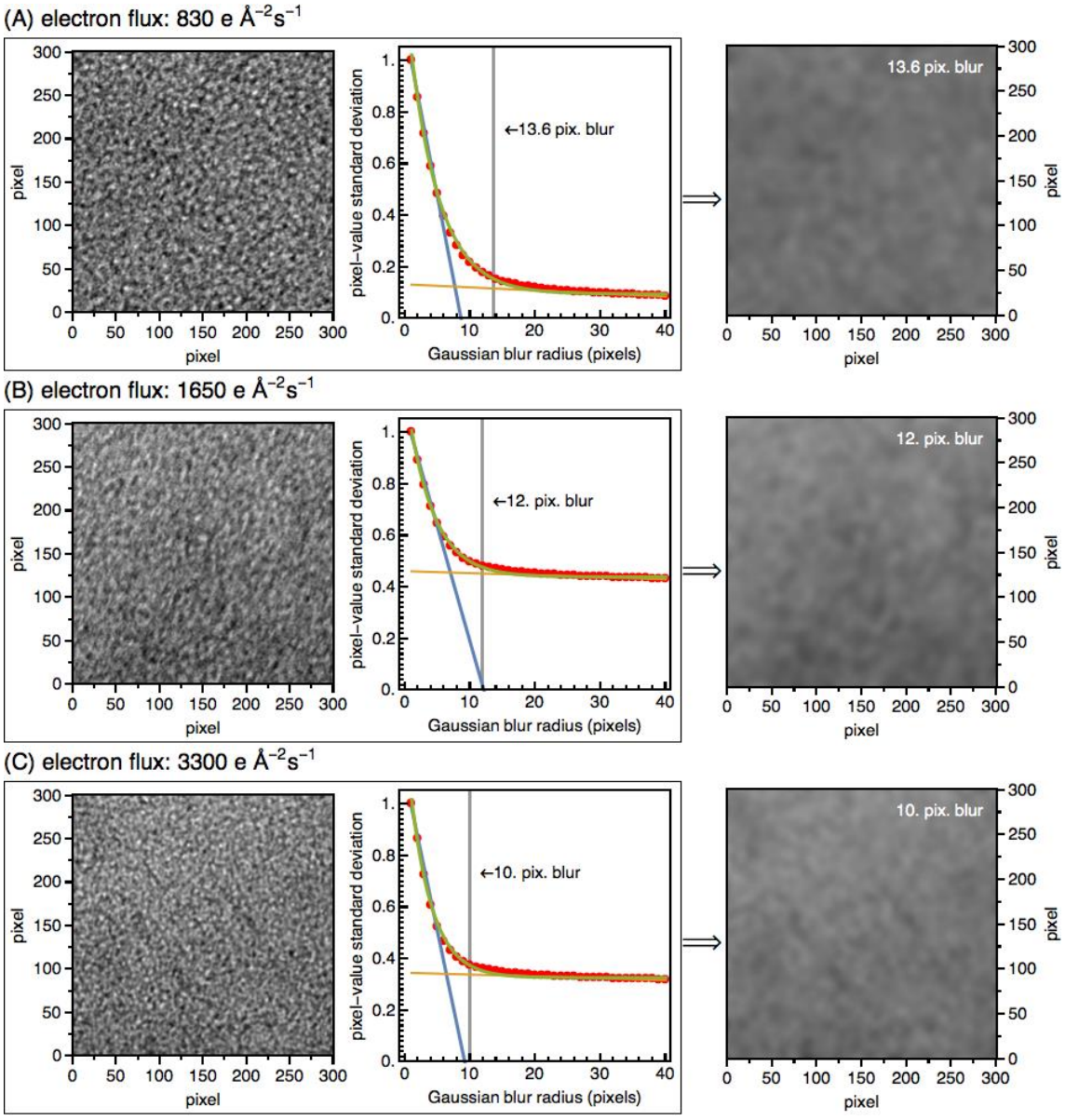

Supp. Fig. 7: Determining a blur-radius for the Gaussian low-pass filter. (Left): A 19.5×19.5 nm^2 patch of background solution contrast was selected at the beginning of each movie. This contrast is primarily a result of scattering from amorphous silicon nitride membranes, disordered liquid and the contrast transfer function of the electron microscope. **(Middle):** Gaussian filters of various pixel widths were applied to the image on the left while we kept track of the standard

deviation of the resultant pixel values (red dots on plot). By fitting an exponential to these points (green curve) we determine the Gaussian blur pixel radius that reduces the standard deviation in the background to 5% unblurred case (thin vertical line on plot). **(Right):** The original image reduced to 5% of the initial standard deviation by a Gaussian filter. This blur-radius is computed once at the beginning of each TEM movie and used for all subsequent frames. This is because the imaging and background conditions fluctuate relatively little throughout our observation of a small field of view.

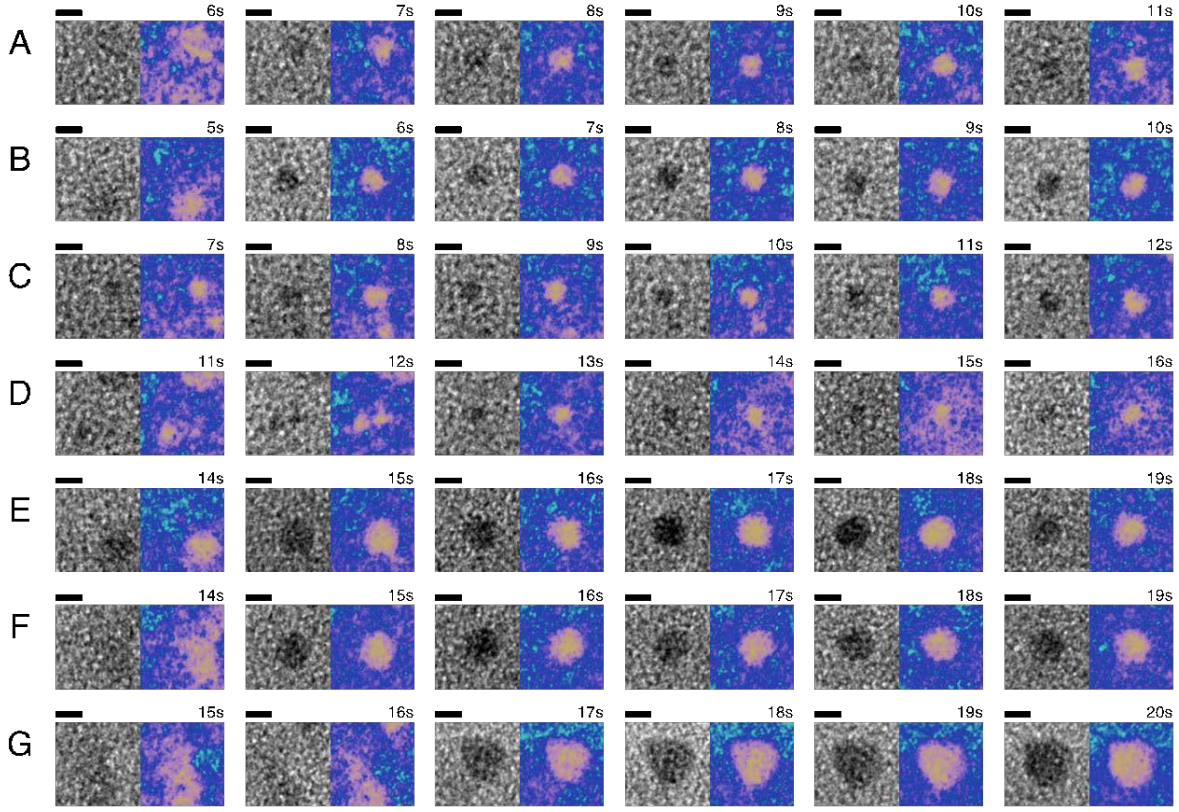

Supp. Fig. 8: Gaussian low pass filter to enhance cluster boundary. A Gaussian low-pass filter of 1.6 nm standard deviation suppresses high-spatial frequency noise from silicon nitride, water and defocus artifacts (these occur at length scales $\leq$ 1.4 nm). In the examples here we have one sequence-pair per double-column, with the grayscale raw TEM sequences adjacent to its post-processed version. The original and low-pass filtered images are averaged equally to produce these post-processed images. Scale bars (2 nm) and time progressions (1 s between frames) are displayed. The low-pass filter enhances features/regions of extended high mass densities, while averaging away uncorrelated and random spatial densities from noisy artifacts. Our cluster sizing algorithms are based these low-pass filtered results. ***All nanoclusters considered in this manuscript were tracked contiguously for at least 5s, to avoid fluctuating features that are spurious***. See Supp. Fig. 7 for more on how we selected our Gaussian filter.

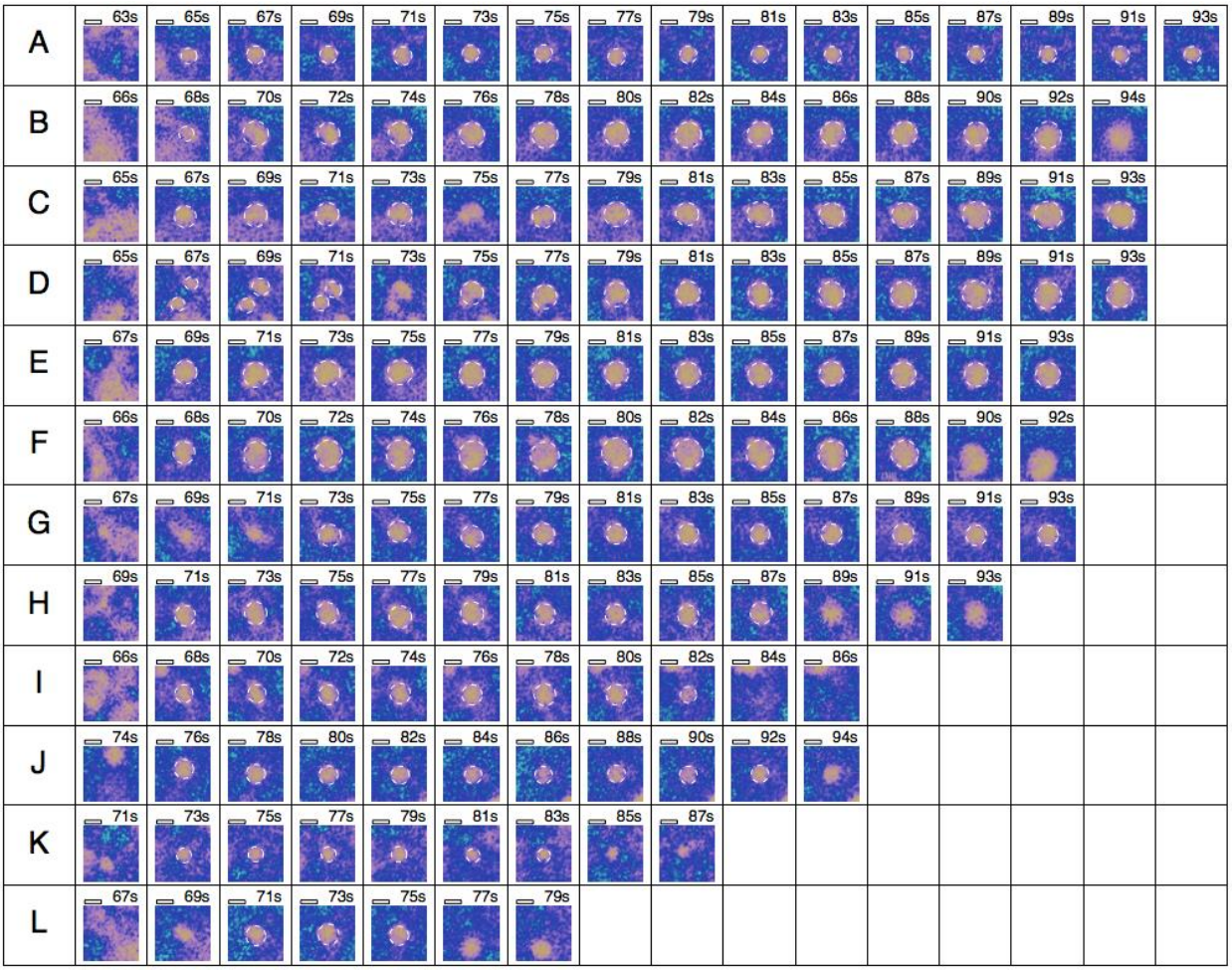

Supp. Fig. 9: Tracking cluster boundaries in low-pass-filtered TEM images. Here we show how gold nanoclusters are sized in the low-pass-filtered TEM micrographs. The full TEM field of view is low-pass-filtered (using a Gaussian filter with 0.9 nm standard deviation, as determined in Supp. Fig. 7A) to identify candidate nanoclusters. A "decimated identification" is adopted: we attempt to identify nanoclusters at every 10^{th} frame of the full sequence (or 1 s intervals since raw movies were recorded at 10 Hz by the TEM's camera). Candidate nanoclusters are further examined only if their boundaries overlap between these consecutive "decimated frames" and persist for longer than 5 s. In this figure, we superimpose white semicircles on magnified regions around each of single nanoclusters whose morphologies are compact, not connected to the borders of the segmented image, and are at least 0.6 nm across in diameter and have elongation factors (i.e. 1-width/height) less than 0.6. If present, the white semicircles on each cluster have the same radius as an equivalent disk that shares the same area as each digitally segmented cluster.

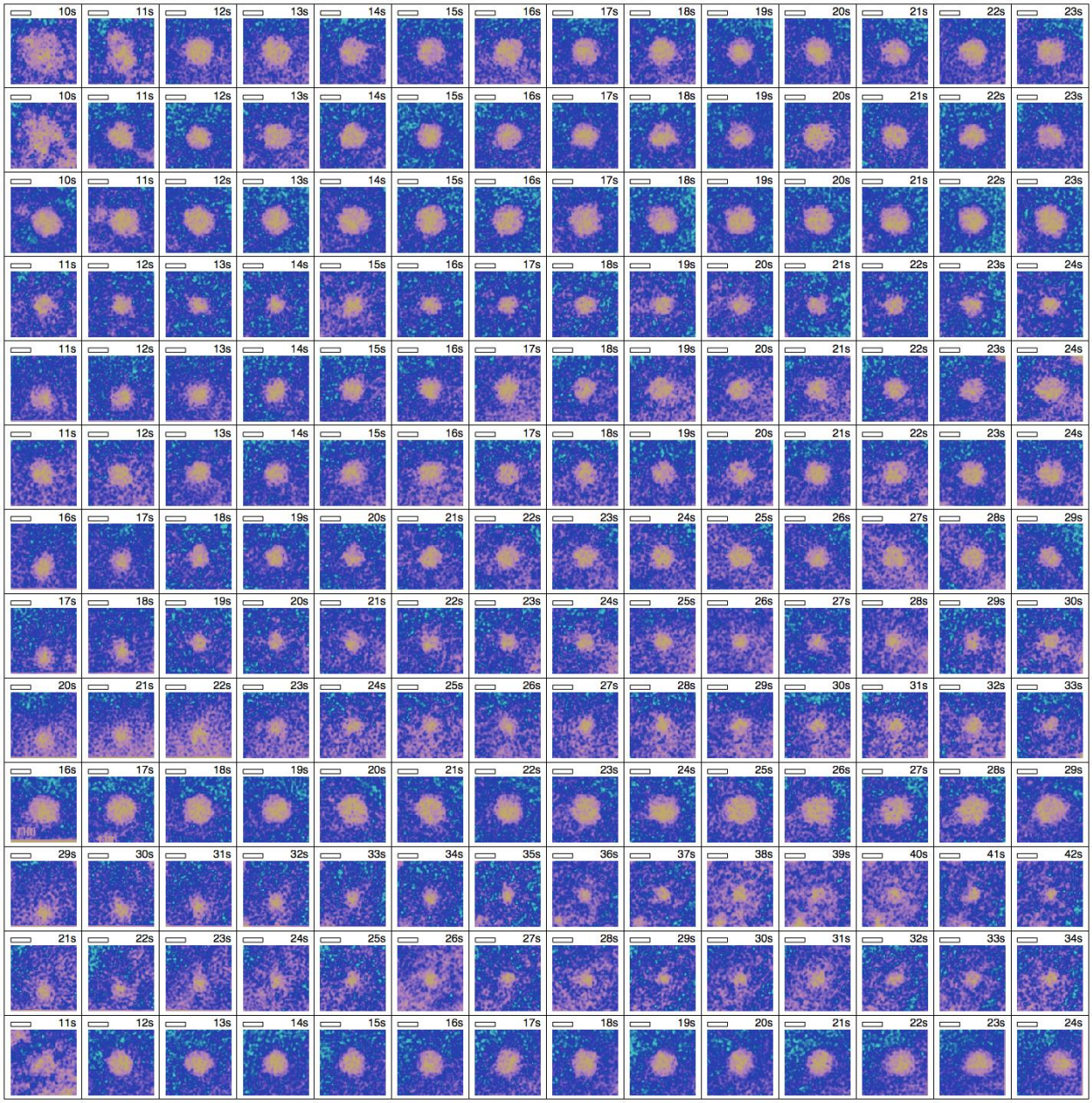

Supp. Fig. 10: Array of gold nanoclusters observed. Each image shows a 65.3×65.3 Å^2 field of view (100×100 pixel^2) re-centered around a cluster's approximate centroid in the final frames (2 nm scale bar on the top left of each panel). Notice that many of the nanoclusters persist for 10 s or longer.

Supplementary Section 9. Crystallinity score.

This section describes our attempt to compute a crystallinity score that is robust against the imaging artifacts (defocus and spherical aberration) expected in TEM images, and background contrast (e.g. silicon nitride membranes, and weakly scattering water molecules in the TEM liquid cell). The idea here is to be able to detect the lattice planes of a nanocrystal when they rotate into view. The appearance of lattice planes in the TEM image has a strong signature in the image's Fourier transform where intensity peaks appear, not unlike Bragg peaks in crystallography that are modulated by the nanocrystal's shape transform (Supp. Fig. 11). For sufficiently thin samples, this Fourier transform is equivalent to the kinematic diffraction of thin samples in the field of view, multiplied by intensity modulations due to the electron beam's phase profile.

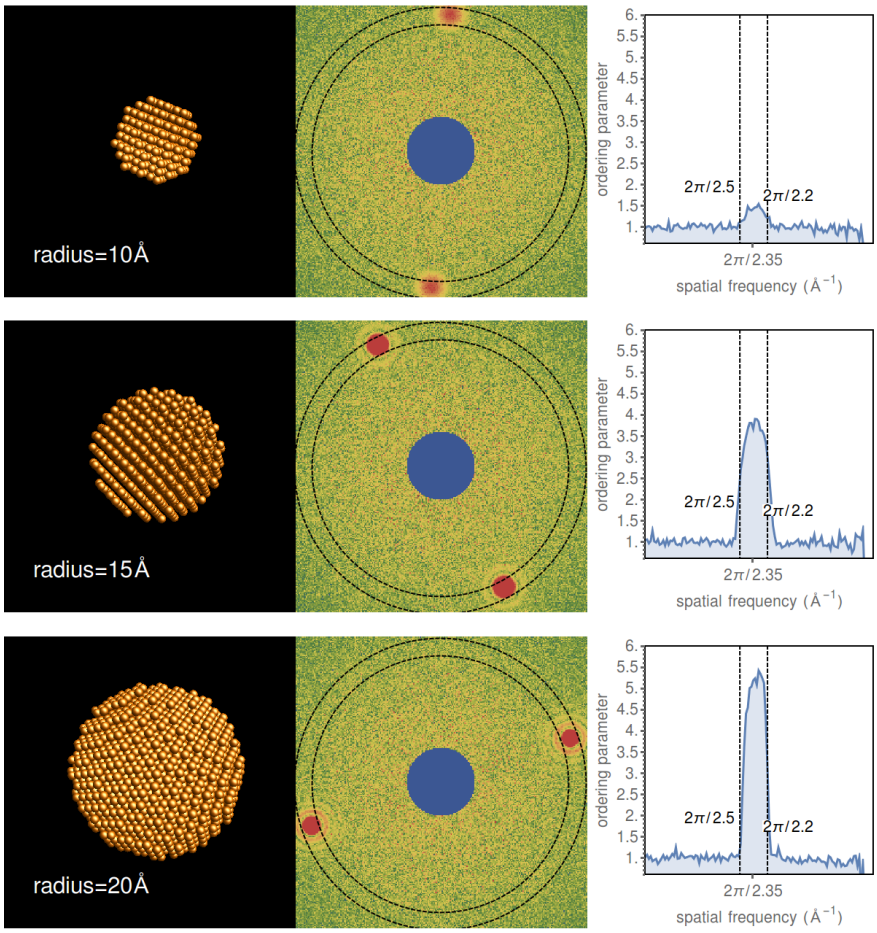

Supp. Fig. 11: Crystallinity score and the ordering parameter. (**Left column**) Simulated Face-Centered Cubic (FCC) gold balls of various radii. (**Middle column**) Simulated kinematic diffraction pattern from each randomly rotated crystal. To this we added Fourier intensities of a random scatterer to simulate uncorrelated background contrast. A "virtual beamstop" (blue) blocks off the central intensities for better contrast rendering. The Bragg-peaks are modulated by the crystal's shape transform and generally decrease in size in reciprocal space with larger crystal radii. The black rings mark the spatial frequencies $2\pi/2.5$ and $2\pi/2.2$ Å^{-1}; the {111} FCC Bragg peak occurs at $2\pi/2.35$ Å^{-1}. (**Right column**) Ordering parameters computed from these diffraction patterns typically fluctuates around unity (Supp. Eq. 29), with peaks between spatial frequencies $2\pi/2.5$ and $2\pi/2.2$ Å^{-1} where the {111} Bragg peak appears. ***The crystallinity score is defined as the average ordering parameter between spatial frequencies $2\pi/2.5$ and $2\pi/2.2$ Å^{-1}*** (black dashed lines).

Fourier intensities of the rotationally-symmetric disorded background in images along fixed spatial resolutions $F(|k|)^2$ are well approximated by exponential distributions, similar to uncorrelated scatterers in Wilson *et al.*[18] A property of exponential distributions is that the ratio of their standard

deviation σ to average μ is close to unity (see rightmost columns in Supp. Fig. 11). Assuming that these exponential distributions are intrinsic to the disorder of the background of uncorrelated scattering densities, deviations from an exponential distribution occur when a subset of the Fourier intensities $F(|k| = k_{\mathrm{ord}})^2$ include bright Bragg-like reflections that arise from crystalline domains. In these cases, the defined ordering parameter,

$$\tilde{\sigma}(k) = \sigma(k)/\mu(k), \qquad \text{(Supp. Eq. 24)}$$

$$\text{where } \mu(k) = \langle F(\boldsymbol{k})^2 \rangle_{|\boldsymbol{k}|=k}, \quad \text{and} \quad \sigma(k) = \left(\langle |F(\boldsymbol{k})^2 - \mu(k)|^2 \rangle_{|\boldsymbol{k}|=k} \right)^{1/2},$$

also exceeds unity appreciably. Notice that the ordering parameter in Supp. Eq. 24 is independent of the average intensity level at each spatial resolution, $F(|k|)^2$, and less susceptible to defocus artifacts expected in TEM images.

The crystallinity score is defined as the average ordering parameter between spatial frequencies 2π/2.5 and 2π/2.2 Å^{-1}, $\langle \tilde{\sigma}(2.52 < k < 2.85) \rangle$. Supp. Fig. 12 compares the ordering parameter and crystallinity scores for a cluster showing diffraction contrast versus background-only contrast. Supp. Fig. 13 shows how we computed the baseline crystallinity scores for non-crystalline, amorphous background-only contrast: *a cluster with a crystallinity score beyond this baseline distribution gives us 99.9% confidence in ascribing it crystalline*. High crystallinity views of some nanoclusters are shown in Sup. Figs. 14-16.

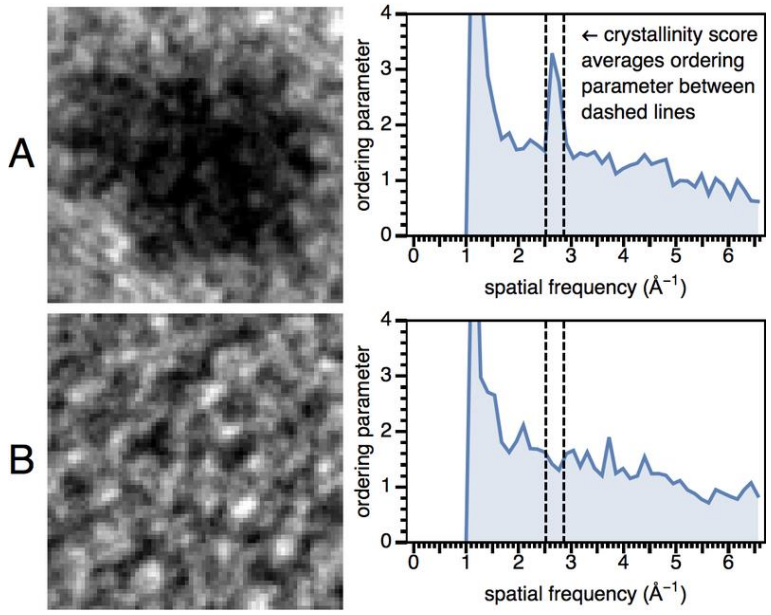

Supp. Fig. 12: Steps involved in computing the crystallinity score of a cluster. (**A**) In the left panel, we first extract a 46×46 Å^2 field of view (71×71 pixel^2) centered on a cluster's approximate centroid. These cropped images were not processed in any other way. From the Fourier intensities of this cropped view, $F(|k|)^2$, we compute the ordering parameter, $\tilde{\sigma}(k)$ shown in the right panel. The crystallinity score is the average value of the ordering parameter between spatial frequencies k = 2π/2.5 to 2π/2.2 Å^{-1} (range shown between dashed vertical lines). (**B**) The same steps in (A) performed for background only TEM contrast (i.e. silicon nitride + water), without gold nanoclusters.

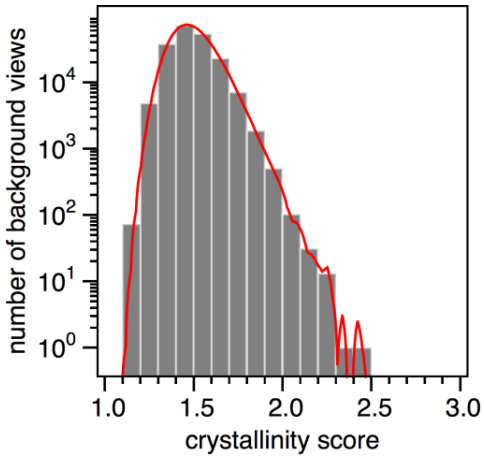

Supp. Fig. 13: Crystallinity score of background contrast. Histogram of crystallinity scores for background only scatterers (silicon nitride + water), similar to Supp. Fig. 12B. We randomly selected 200,000 46×46 Å^2 square regions in 300 TEM images that do not show any gold nanoclusters. The crystallinity score was computed for each one of these background images, as prescribed in Supp. Fig. 12, and shown here as a histogram. To this histogram, a smoothed kernel distribution was fitted using 50 interpolation points (red curve), which also superimposes the right panel of Figure 3 of the main text.

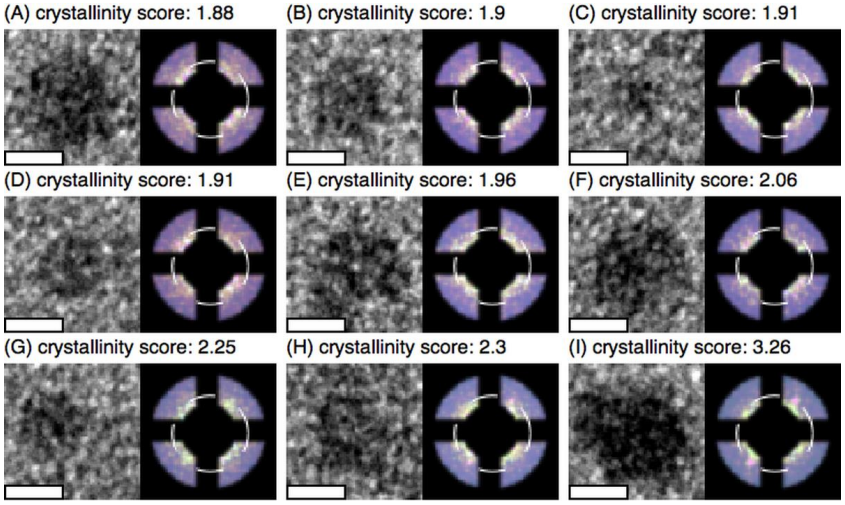

Supp. Fig. 14: Highest crystallinity scores achieved by each cluster, for some of the nanoclusters observed at 830 e Å^{-2} s^{-1}. Panels show the TEM image (46×46 Å^2 region, with 2 nm white scale bar) and the image's Fourier intensities (suitably masked; the white dashed line shows where the crystalline gold's FCC {111} peak should occur). (**A-E**) Particles that do not show statistically significant crystallinity above background. (**F-I**) Particles that show diffraction contrast from atomic lattice planes also show peaks in their Fourier transforms within the masked region.

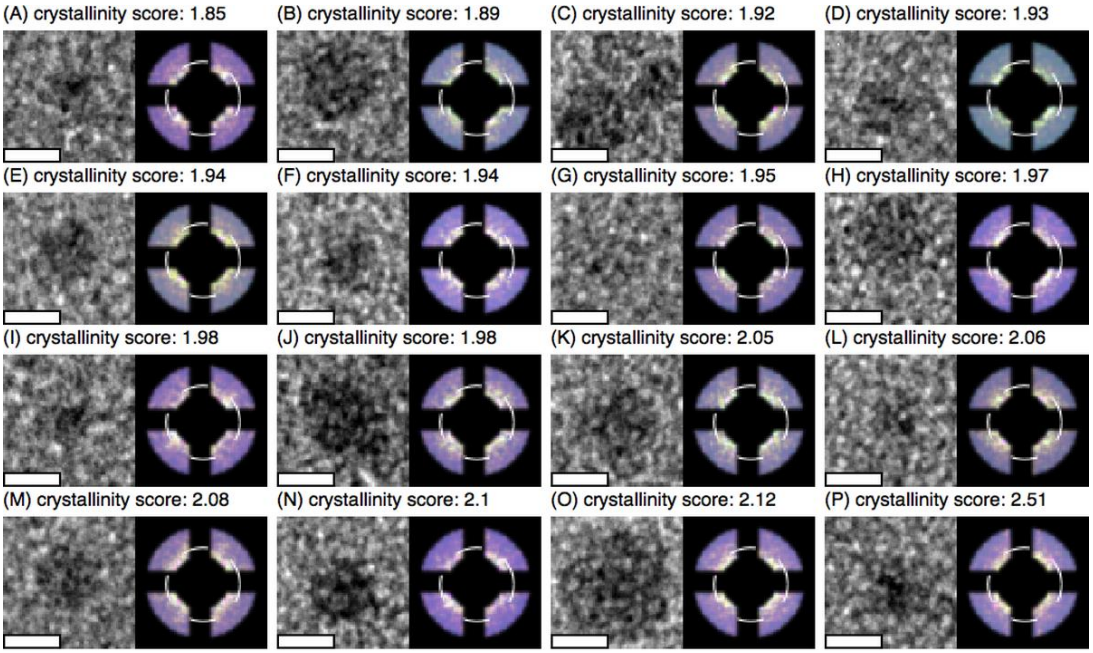

Supp. Fig. 15 Highest crystallinity scores achieved by each cluster, for some of the nanoclusters observed at 1650 e Å^{-2} s^{-1}. Similar to Supp. Fig. 14; TEM images are shown (46×46 Å^2 region, with 2 nm white scale bar) together with their masked Fourier transforms. (**A-J**) Particles that do not show statistically significant crystallinity above background. (**K-P**) Particles that show significant crystallinity.

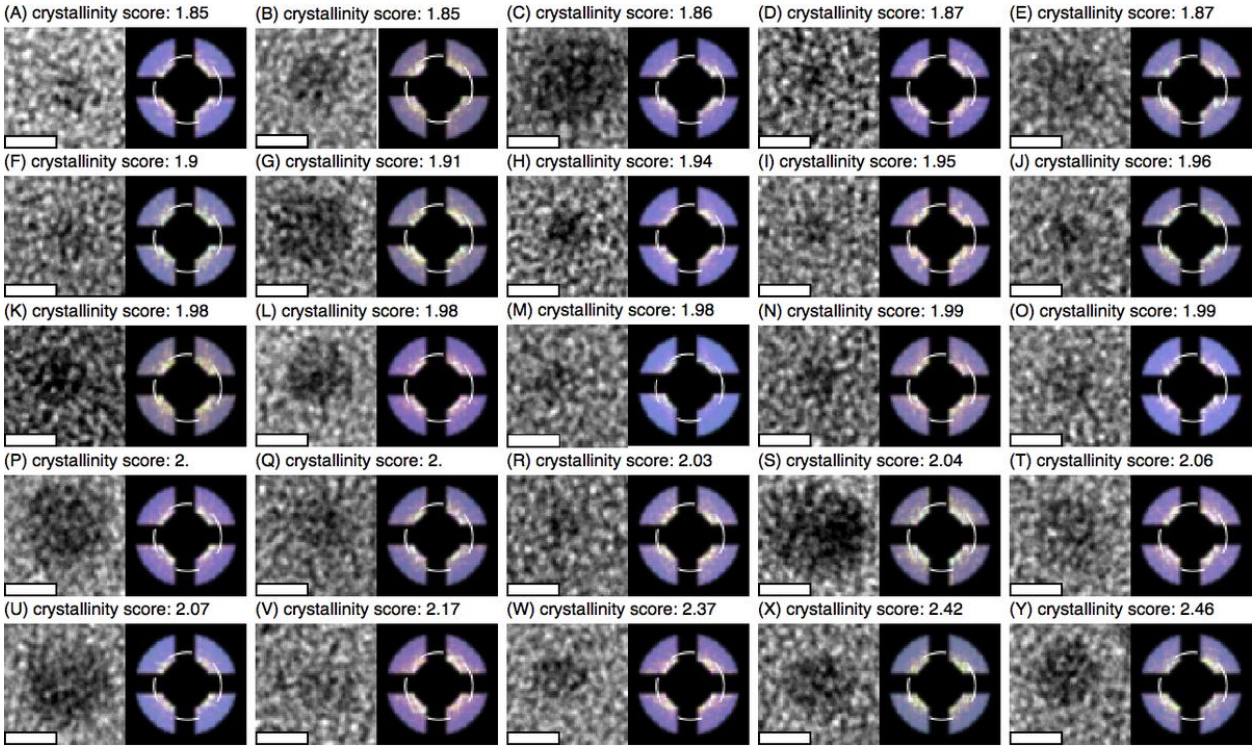

Supp. Fig. 16: Highest crystallinity scores achieved by each cluster, for some of the nanoclusters observed at 3300 e Å^{-2} s^{-1}. Similar to Supp. Figs. 14 and 15, TEM images are shown (46×46 Å^2 region, with 2 nm white scale bar) with their Fourier transforms. (**A-O**) Particles without statistically significant crystallinity above background. (**P-Y**) Particles with significant crystallinity.

Supplementary Section 10. Cluster diffusion in bulk water given Stokes-Einstein relation.

The Stokes-Einstein two-dimensional diffusion of spherical objects of radius r in a viscous medium of dynamic viscosity η, at temperature T has a diffusion coefficient of

$$D = k_B T/(6\pi\eta r). \quad \text{(Supp. Eq. 25)}$$

For r = 1 nm spherical particles in bulk water, $\eta = 9\times10^{-4}$ Pa s at 22 °C, its diffusion coefficient is $D \sim 10^{-10}$ m^2 s^{-1}, which is about nine orders of magnitude lower than that observed in Figure 2c in the main text. See Supp. Fig. 17 for a more quantitative fit. This is consistent with diffusion coefficients reported by Lu *et al.*[2]

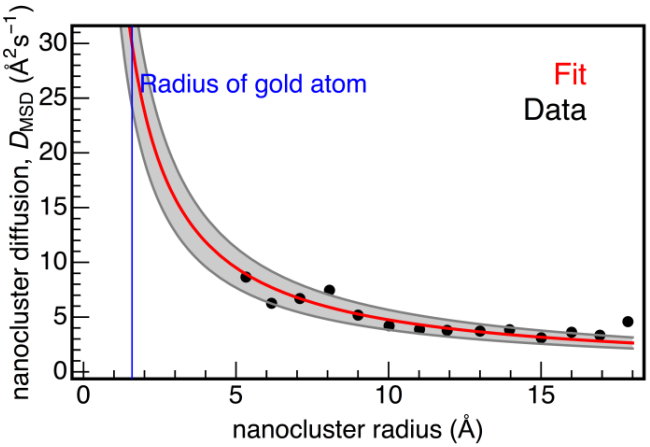

Supp. Fig. 17: Fitting Supp. Eq. 25 to average diffusion coefficients against particle radius, combined for all three electron dose rates in Figure 2. We find an apparent diffusion coefficients at 295.15 K to be ~4×10^9 times less than in bulk water. The gray curves show the 99.9% mean confidence bands of the fit shown in red.

Supplementary Section 11. Comparisons with nucleation parameters in literature.

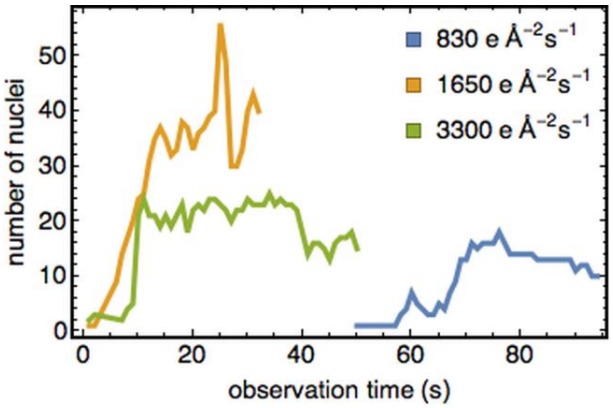

Supp. Fig. 18: Nucleation rate versus electron dose rate. Here we track the number of persistent nanoclusters in Figure 2 of the main text. The number of nanoclusters fluctuate because they coalesce, exit the field of view or are temporarily obscured by the strongly scattering gold-rich liquid phase. The nucleation rates here are limited by the production of neutral gold and the rate of spinodal decomposition, which in turn depends on molecular diffusion rates of gold in water. Hence, the maximum nucleation rate from liquid gold phase should be at least as fast as that in the high dose rate case, or > 10^{21} m^{-3}s^{-1} (within the 54×54×30 nm^3 observation volume in the liquid cell).

Classical nucleation theory (CNT) describes how matter in one phase nucleates out of another. The Gibbs free energy thus comprises a term that scales as the volume of the nucleating phase, and another that scales as interfacial surface between the two phases:

$$\Delta G(r,T) = -g_{vol}(T)\,\frac{4\pi r^3}{3} + \sigma_{12}(T)\,4\pi r^2, \quad \text{(Supp. Eq. 26)}$$

where the nucleating phase assumes a sphere of radius r in an isotropic system. Two system-specific fit parameters in this free energy are its temperature-dependent free energy per unit volume, $g_{vol}(T)$,

and the interfacial energy between the two phases, σ_{12}. CNT makes predictions about two primary observables that are often compared with experimental and simulation results: the critical nuclei size (at which $\Delta G(r,T)$ reaches a maximum) beyond which the nuclei are stable and monomers can attach (the energy penalty for monomer addition is lower than the energy penalty for the increase in solid-liquid surface area), and the nucleation rate (i.e. rate at which critical nuclei are formed). In general, the formation rate of critical nuclei, J, varies exponentially as the cube of the interfacial energy:

$$J \propto \exp(-C\ \sigma_{12}(T)^3/k_BT), \qquad \text{(Supp. Eq. 27)}$$

where C is nucleation model-dependent dimensionful parameter. Hence the interfacial energy is a more sensitive fit parameter to CNT's prediction of nucleation rates. If in our TEM observations each distinguishable nanocluster forms from a single nucleus, and that nanoclusters form in a well-separated fashion at early times and coalesce only later on, we can then estimate nucleation rates from Supp. Fig. 18 to within an order of magnitude. In what follows, these nucleation rates are used to fit the interfacial energy of crystalline gold nucleating out of either an aqueous solution or a liquid melt.

The nucleation rates observed in Supp. Fig. 18 represents a lower bound of what we should expect since we are diffusion-limited in the liquid cell. From Supp. Eq. 27, this implies that can only determine the upper bound on the interfacial energy σ_{12} by fitting to rates in Supp. Fig. 17.

Supp. Figs. 8-10 suggest a multi-step nucleation process, where early stage gold-rich regions are liquid with fluid-like morphologies that eventually compactify and display crystallinity. Sub-section Supplementary Section 11A records CNT's description of how a dense gold-rich liquid phase nucleates from an aqueous solution of gold solutes, while sub-section Supplementary Section 11B describes how a solid phase nucleates from this dense liquid phase.

Supplementary Section 11A. Step 1: gold nucleating out of an aqueous solution.

LaMer and Dinegar proposed the *burst nucleation model* to explain how nuclei that condense from solution are relatively monodisperse.[19] The non-classical idea is that nucleation depletes the local concentration of solutes, thus violating the constant concentration assumption in the classical nucleation model. This arrests the growth of nuclei, which makes for a more monodisperse dispersions. This burst nucleation model has been quantified by Privman *et al.*,[20] who applied this to the nucleation of gold aggregates from solution.[21] In his model, the Gibbs free energy for a gold-dense embryo nucleating out of an aqueous solution is

$$\Delta G(n,T) = -n\,k_BT\log(c/c_0) + 4\,\pi a^2 n^{2/3}\,\sigma_{\mathrm{Au+W}}(T), \quad \text{(Supp. Eq. 28)}$$

with the following definitions: n is the number of gold atoms in the embryo at temperature T; c is the gold concentration in the aqueous solution (ranges from 0.2 M in Figure 2b to 4 M Supplementary Section 5); c_0 is the saturation concentration of Au solutes in solution at room temperature, 10^{15} m^{-3};[22] the atomic gold radius a is taken as 1.6 Å; and the interfacial energy between water and a gold-only embryo $\sigma_{\mathrm{Au+W}}(T)$ is our fit parameter. The only an approximate order of magnitude for c_0 is needed in the calculations below since c_0 always appears within a logarithm. The enthalpy term is neglected in Supp. Eq. 28, as was done by Privman *et al.*,[21] which assumes that the formation of embryo in burst nucleation is essentially entropically driven by non-interacting solutes. We will revisit this assumption at the end of this section.

The critical nuclei occurs when the Gibbs free energy is a maximum with respect to n, and further addition of atoms only decreases this free energy. The number of gold atoms and Gibbs free energy of this critical nuclei are respectively:

$$n_{\text{crit}} = \left(\frac{8\pi a^2 \sigma_{\text{Au+W}}}{3k_B T \log(c/c_0)}\right)^3, \quad \text{(Supp. Eq. 29)}$$

$$\Delta G_{\text{crit}}(\sigma_{\text{Au+W}}, c, T) = \frac{256\pi^3 a^6 {\sigma_{\text{Au+W}}}^3}{27\,(k_B T \log(c/c_0))^2}. \quad \text{(Supp. Eq. 30)}$$

The nucleation rate in Supp. Fig. 17 depends on the diffusion-limited capture rate of dissolved solutes, and the free energy barrier for the additional solute to stick. These two effects are multiplied to give a nucleation rate of

$$J(\sigma_{\text{Au+W}}, c, T) = \left(4\pi a {n_{\text{crit}}}^{1/3} D_{\text{Au}} c\right)\left(c e^{-\Delta G_{\text{crit}}(\sigma_{\text{Au+W}}, c, T)/k_B T}\right), \quad \text{(Supp. Eq. 31)}$$

where D_{Au} is the diffusion coefficient for gold solutes in solution, which is extrapolated from the average radii and diffusion coefficients of nanoclusters in Figure 2c to molecular diffusion of gold using the Stoke's Einstein diffusion equation in Supp. Eq. 25 in Supplementary Section 10. These diffusion coefficients turn out to be 45 and 48 Å^2 s^{-1} for imaging fluxes of 830 and 1650 e Å^{-2} s^{-1}, respectively.

In fitting for interfacial energy $\sigma_{\text{Au+W}}$ in Supp. Eq. 31 to nucleation rates in Supp. Fig. 18, the primary uncertainties lie with that of gold solute concentration during nucleation, c, and the temperature of the system. The lower and upper limits of c was estimated from Figures 2c and Supplementary Section 5 respectively. Since we did not have a direct measurement of the temperature of the liquid cell, we were more generous with its upper limit, doubling that which was computed in Supplementary Section 3. Scenarios for various electron dose rates, the upper and lower limits of temperature and solute concentration are plotted in Supp. Fig. 19. We find that the $\sigma_{\text{Au+W}} \leq 0.6$ N m^{-1}, which agrees tentatively with Privman's attempt to fit this interfacial energy (0.57 ± 0.04 N m^{-1}) to the coagulation of micron-size colloids from "burst nucleation" of primary gold nanoparticles.[21]

There is indirect evidence that the nucleated phase is non-crystalline. The critical nucleus with interfacial energy $\sigma_{\text{Au+W}} \leq 0.6$ N m^{-1} in Supp. Fig. 19 has fewer than one atom. Hence, it is meaningless to assign the nucleus as solid or liquid, or distinguish if surface from bulk gold atoms. The critical nuclei in this condition is clearly a stark artificiality of CNT. Because we observe fluid-like gold-rich phase in Figure 2A or those shown in Supplementary Section 8, we conclude that there must be a second nucleation step that crystallizes these liquid phases. We note that the smooth necks between fused gold nanoparticles that nucleated from solution studied by Privman *et al.*[21] may have suggested multiple steps in its nucleation.

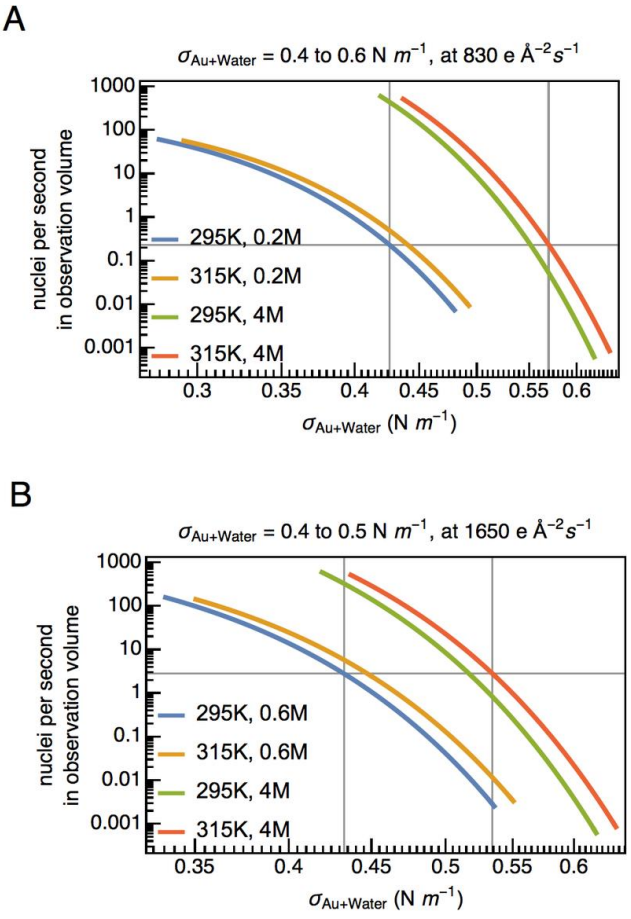

Supp. Fig. 19: Estimating surface tension between gold and water from nucleation rates in Supp. Fig. 18. (**A**) Using the average diffusion coefficients of nanoclusters at 830 e $Å^{-2}$ s^{-1}, we estimate a possible range of interfacial energies between gold and water given a nucleation rate of ~ 0.23 nuclei s^{-1} (measured in Supp. Fig. 18) within the observation volume of 54×54×30 nm^3. The range of Au densities in the solution is bounded from below by Figure 2C in the main text, and bounded from above by STEM measurements in Supplementary Section 4. We find $\sigma_{Au+Water}$ to be between 0.4 and 0.6 N m^{-1} at this nucleation rate (gray cross hairs). (**B**) Same as (A), but at 1650 e $Å^{-2}$ s^{-1} and with a nucleation rate of ~ 2.8 nuclei s^{-1} (measured in Supp. Fig. 18). Here $\sigma_{Au+Water}$ is between 0.4 and 0.5 N m^{-1} (gray cross hairs).

We revisit our assumption that the enthalpic term of a nanocluster can be ignored in Supp. Eq. 28. Figure 4 in the main text indicates that this enthalpic term should be negative and closer to -10 kcal/mol since we know that the metastable gold-rich aqueous phase is still internally hydrated. This results in an enthalpic term that is approximately $-8nk_BT$, and is about a 30% that of the entropic term of $-28nk_BT$ in Supp. Eq. 28. If we assumed that the Au-Au cluster were dehydrated in Figure 4, this enthalpic term would grow to around ~ $30nk_BT$ and start to match the entropic term. In either case adding the enthalpy term only shrinks the size of the critical nuclei, and does not change the fact that said nuclei is still smaller than a single atom. It also reinforces the assumption that the enthalpic term, which involves at least two gold atoms, can be dropped. Ultimately, the application of CNT here remains ambiguous and the structure of this nuclei is ill-defined.

Supplementary Section 11B. Step 2: gold crystallizing out of amorphous nanoclusters.

Here, we consider the possibility that the crystallization of atoms in amorphous nanoclusters can be approximated by the crystallization of liquid gold melt. We find support for this in three observations. First, from the crystallinity scores in Figure 3 we know that many nanoclusters are internally amorphous. Second, the early stage fluid-like boundaries of nascent nanoclusters in Figure 2a also suggest that the amorphous nanoclusters are internally disordered, not unlike those in a liquid phase. Third, the fact that these amorphous nanoclusters eventually crystallize also indicates their internal restructuring, which is again similar to how atoms in liquid gold reconfigure.

Much like in Supplementary Section 11A, we computed an upper bound on the solid-liquid interfacial energy in gold σ_{sl} using an estimated crystallization rate. According to the capillary approximation in the classical nucleation theory,[23,24] the Gibbs free energy of a spherical solid gold cluster of radius r in a liquid melt at temperature T is

$$\Delta G(r,T) = \Delta G_{\text{bulk}} + \Delta G_{\text{surface}} = \frac{4\pi r^3}{3}\frac{\Delta H_{\text{fusion}}\,(T_{\text{m}}-T)}{T_{\text{m}}} + 4\pi r^2\sigma_{sl}(T), \text{ (Supp. Eq. 32)}$$

with the following definitions and assumptions: the melting point of gold, T_{m}=1337.3 K; ΔH_{fusion} = -1.2 ×10^9 J m^{-3} is the enthalpy of gold per volume (equivalent to -12.3 kJ mol^{-1}); and the temperature within the liquid cell T = 295.15 K; the surface tension between solid and liquid gold, $\sigma_{sl}(T)$. The temperature-dependent solid-liquid surface tension $\sigma_{sl}(T)$ in Supp. Eq. 32 is a crucial quantity that is very difficult to measure in liquid-to-solid nucleation. This surface tension is typically regarded as a fit parameter adjusted to account for experimental[25,26] or simulated[27–29] observations.

Two quantities that are typically computed in CNT are tested by experiments. First, the solid nucleus's critical radius occurs when the surface and bulk energies are equal in Supp. Eq. 32, which leads to

$$r_{\text{crit}}(\sigma_{sl},T) = -\frac{2\,\sigma_{sl}(T)\,T_{\text{m}}}{\Delta H_{\text{fusion}}\,(T_{\text{m}}-T)}. \quad \text{(Supp. Eq. 33)}$$

The Gibbs free energy of a nucleus at this critical radius is,

$$\Delta G_{\text{crit}}(\sigma_{sl},T) = \frac{16\pi}{3}\left(\frac{T_m}{T_{\text{m}}-T}\right)^2\frac{\sigma_{sl}(T)^3}{\Delta H_{\text{fusion}}{}^2}, \quad \text{(Supp. Eq. 34)}$$

which increases rapidly as the third power of the surface tension. The second oft-compared quantity in CNT is the nucleation rate

$$J(\sigma_{sl},T) = Z\,f(n_c)\,\rho\,\exp(-\Delta G_{\text{crit}}(\sigma_{sl},T)/k_BT), \quad \text{(Supp. Eq. 35)}$$

where Z is the Zeldovich factor that denotes the probability of a nucleus to form at the top of the free-energy barrier ($n = n_c$), which is $\sqrt{(-\frac{1}{2\pi k_BT}\frac{\partial^2\Delta G(n)}{\partial n^2})} \approx 0.04$; we assumed a gold number density ρ = 5.8×10^{28} m^{-3}; and $f(n_c)$ is the monomer attachment rate for a nucleus with n_c atoms. Again, notice that the nucleation rate in Supp. Eq. 35 depends exponentially on the surface tension to the third power.

The monomer attachment rate $f(n_c)$ of liquid gold molecules onto a solid gold nucleus of radius r can be bounded from above by treating the liquid molecules as non-interacting hard spheres. This hard-sphere approximation allows us to estimate the monomer impingement rate ν using the kinetic theory of ideal gases, $f(n_c) \leq 4\pi r^2\nu$. The impingement rate in an ideal gas,

$$\nu = \frac{p}{\sqrt{2\pi m k_BT}}, \quad \text{(Supp. Eq. 36)}$$

where $p_L = 2\sigma_{sl}(T)/r$ is the Laplace pressure at the surface of the gold nucleus of surface tension $\sigma_{sl}(T)$, m is mass of the gold molecule, and T is its equilibrium temperature. We assume that at steady state, the external pressure due to liquid gold balances the Laplace pressure inside the gold nucleus. This produces an upper bound on the attachment rate on the critical solid nuclei $f(n_c) < 4.1\times10^{13}$ s^{-1}. We get a very similar upper bound by considering non-interacting atoms in a thin liquid shell (thickness equal to diameter of a gold atom) impinging on a spherical solid nucleus all at equilibrium with a thermal bath at temperature T.

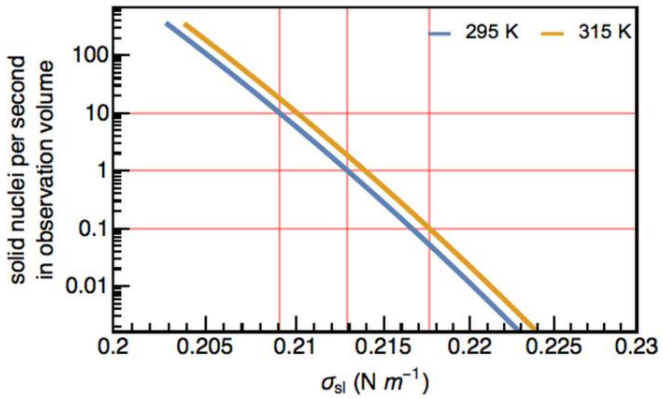

Supp. Fig. 20: Solid-liquid surface tension of gold, σ_{sl}, in the diffusion-capture model. From the average crystallization rate of ~ 0.1-10 nucleus s^{-1} in the field of view (Supp. Fig. 18) $\sigma_{sl} \leq 0.22$ N m^{-1} (red guidelines). Increasing the temperature in the liquid cell by 10 K (twice that expected from estimates in Supplementary Section 3) has little effect.

Estimating the crystallization rate of nanoclusters from our observations is trickier than that of condensation in Supplementary Section 11A. For one, a nanocrystal might not appear crystalline in the TEM either because the diffraction contrast is undetectable against the background, or it has not rotated its lattice planes into view. Furthermore, it is limited by the nucleation rate of nanoclusters in Supplementary Section 11A. Nevertheless, the minimum crystallization rate is likely within an order magnitude of the nanocluster nucleation rates in Supp. Fig. 18: between 0.1-10 crystalline nuclei per second in the observation volume. This lets us bound the interfacial energy between solid and liquid to be $\sigma_{sl} \leq 0.22$ N m^{-1}. Crystallization might go undetectably faster, for reasons earlier in this paragraph, but only if the interfacial energy were lower. Finally, our attachment rate in Supp. Eq. 36 neglects inter-atom attraction and hence gives an upper bound on the nucleation rate. A lower and more realistic attachment rate would also lower our estimated interfacial energy to fit our observed crystallization rates.

The interfacial energy between solid and liquid gold is difficult to measure. This quantity is usually inferred indirectly by fitting experiment or simulations observations to a specific model. A prominent early study by Sambles[25] measured $\sigma_{sl} = 0.27 \pm 0.01$ Nm^{-1} at 1336 ± 2 K from the melting point depression of gold nanoparticles larger than 5 nm in radius in the temperature range 1200-1337 K. Not only were Sambles' nanoparticles substantially larger than those in Supp. Fig. 10, the temperatures were also much higher. This fitted interfacial energies is also specific to a thin liquid shell model, where a solid nanoparticle first melts from the exterior thus creating a thin liquid shell. This model had two fit parameters that were not directly observed: the liquid shell thickness and the interfacial energy between the solid core and its liquid shell. Sambles assumed a liquid shell of 2.2 nm in their model, which is clearly larger than the crystalline nanoclusters in Figure 3. This last point made it impossible for us to adopt Samble's parameters and model to our observations. Samble's resultant interfacial energy is also incorrect for our room temperature system, because Supp. Eq. 35 predicts an astronomical average time of 10^{19} s to form a crystalline nucleus in a typical $54 \times 54 \times 30$ nm^3 observation volume.

In fact, Chushak *et al*.[27] discuss ambiguities in Sambles' study, and found that face-centered-cubic domains can appear in simulated gold melts if the liquid-solid surface tension were instead $\sigma_{sl} =$ 0.11-0.16 N m^{-1}. These numbers were obtained by fitting thermodynamic relations to observations of how melting points of large nanoclusters (n = 459, 1157, 3943, supercooled in molecular dynamics to 700-740 K using the semi-empirical Embedded Atom Model) fall with cluster size.[27] In Chushak's study, the liquid shell model was used to model melting point depression, where a 5 Å-thick liquid shell coats a solid core nucleus. In fact, one obtains an even lower interfacial energy by fitting the simulated nucleation rates obtained from a 1157-atom cluster[27] to the solid-liquid surface tension in Grasany's diffuse interface theory[30] for CNT: $\sigma_{sl} = 0.084$ N m^{-1} and a diffuse layer of 1.2 Å (smaller than the radius of a gold atom) between liquid and solid phases in the nucleus. In these studies, the

solid nanoparticles are not typically Face-Centered-Cubic crystalline, hence should have a lower interfacial energy because they are structurally closer to liquid gold.

Overall, our estimated upper bound for interfacial energy between crystalline and liquid gold is consistent with those derived from simulations using the Embedded Atom Model.[27] However, simulated crystallization were observed in larger nanoclusters within hundreds of picoseconds,[27] consistent with their lower surface tension of 0.11-0.16 N m^{-1} (compare with nucleation rates in Supp. Fig. 20). In fact, an even higher nucleation rate is expected since, our nanoclusters were supercooled to 300 K compared to 700-740 K for those in Chushak's paper (the possibility of electron beam-induced damage is eliminated in Sections SI2 and SI3). The variability in our interfacial tension perhaps echos what Chushak and Bartell admitted:[27] *"Since existing theories of the melting of small particles and the nucleation of crystals in them are far from rigorous, a close agreement between the quasi-thermodynamic and kinetically based free energies cannot be taken for granted"*. Besides knowing that crystallization should occur, we know fairly little about how it actually occurs.

Supplementary Section 12. Comparisons with earlier reports of spinodal decomposition.

Remarkably, the initial gold concentration, $c_i^{(Au)} \sim 1$ M, is ten orders of magnitude higher than the saturation concentration of gold in aqueous solution (10^{15} m^{-3}) and three orders of magnitude lower than in liquid gold. At 293 K (1044 K below the melting temperature of gold at 1 atm) $c_i^{(Au)}$ could already be in the spinodal region for dilute and liquid Au, where the solution is unstable against concentration fluctuations because of the negative curvature of the Gibbs free energy, $\frac{\partial^2 G}{\partial c^2} < 0$.

To appreciate the features we expect to observe in spinodal decomposition, we simulated this process using the cell-dynamical-systems iterative model described by Oono *et al*.,[31] for the case where the mean-field order parameter (different from the ordering pararmeter in Supplementary Section 9) is conserved. This model employs an *ansatz* iterative map that allows us to one to obtain features similar to spinodal decomposition when precise free-energy functional are absent. Early stage demixing in our simulation Supp. Fig. 21 resembles those observed in Supp. Fig. 22 of solution into gold-rich and gold-poor regions.

There is evidence that our system should undergo spinodal decomposition. Mikhlin *et al.*[32] showed that nucleation of tetraaurochlorate experiments via citrate-synthesis contain liquid-phase precursors hypothesized to form by spinodal decomposition. These liquid-domains were very similar to the ones observed in the crystallization of lysozyme,[33] for which two-step nucleation via spinodal decomposition was proposed. Importantly, these studies were conducted via atomic force microscopy and dynamic light scattering, methods that do not involve ionizing radiation. These same liquid-domains persisted when Mikhlin and co-worked imaged the same preparation with X-rays and electrons.

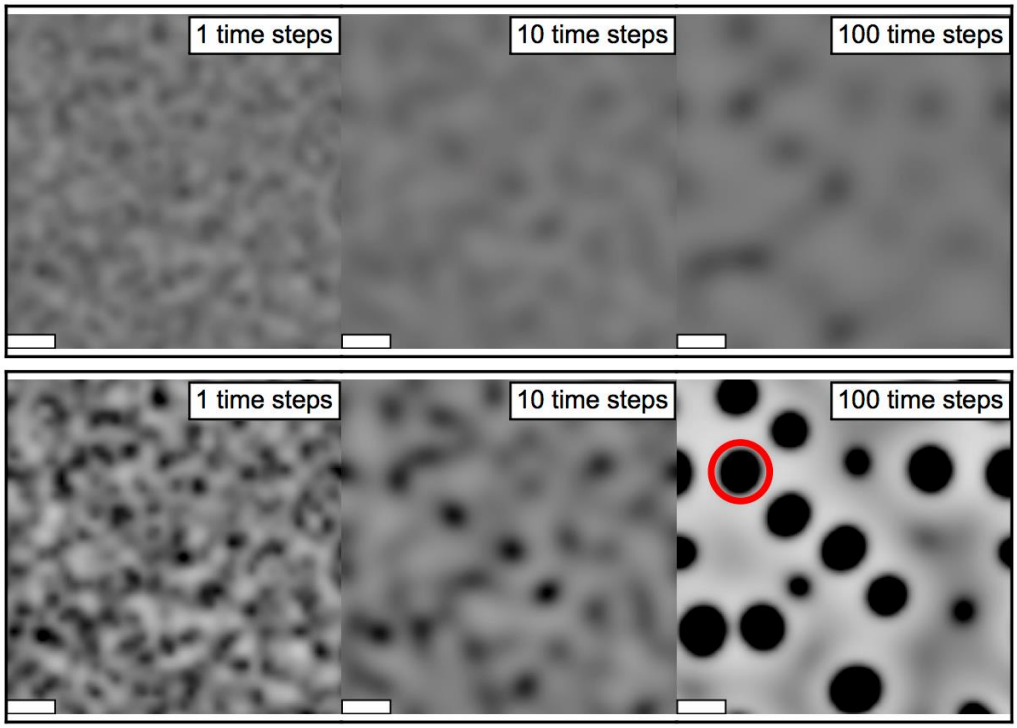

Supp. Fig. 21: Cell-dynamical spinodal decomposition for different solute concentrations. The different rows show the time evolution of spinodal decomposition for different initial concentrations of solute (darker regions) in solution (white regions). The solute concentration in the second row is higher than that in the first row. Notice that the spinodal structures here coarsen, instead of collapsing. A good example is the dense and compact region circled in red, which grows with time until a stable structure is obtained. These dense structures can merge to form larger ones but do not shrink like those in Supp. Fig. 22**.**

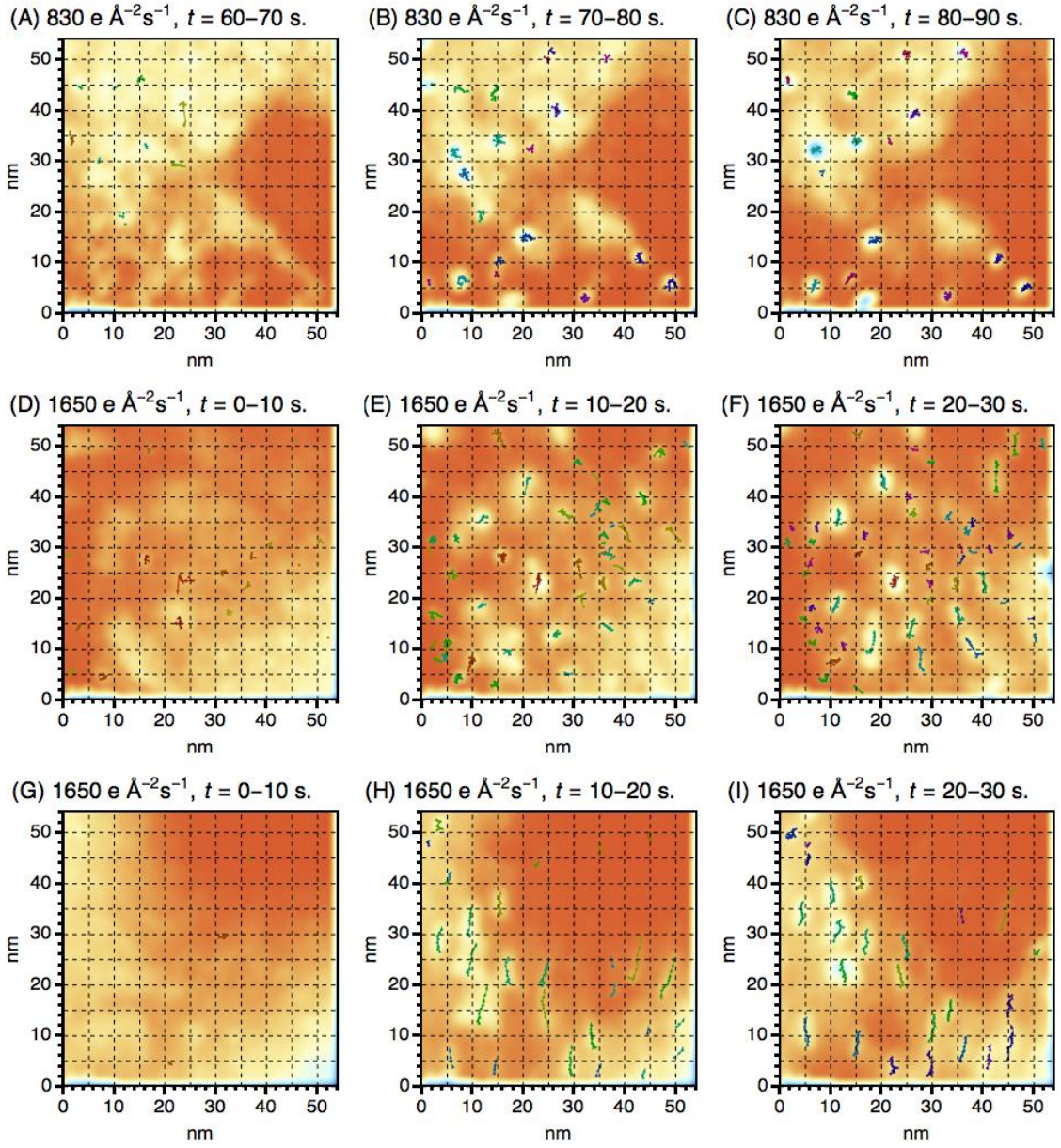

Supp. Fig. 22: Gold nanoclusters nucleate from gold-dense liquid regions. TEM movies of three nucleation sequences acquired with different electron fluxes: (**A-C**) 830, (**D-F**) 1650 and (**G-I**) 3300 e Å^{-2} s^{-1}. Time-averaged TEM micrographs colored yellow and orange for gold-rich and gold-poor regions respectively, are superimposed with centroid trajectories of detectable gold nanoclusters (displacements shown with lines, colored by cluster label). Each cluster's trajectory is decomposed into a sequence of displacements spanning at least 0.2 s.

Supplementary Section 13. Ab initio calculations of a hydrated gold pair.

In order to understand how the spinodal decomposition and delayed gold nucleation takes part in the experiments, we performed quantum and classical atomistic simulations of hydrated gold atoms, and, for simplicity, disregarded other potential chemical components present in the system, mentioned above. First, we performed *ab-initio* calculations of two hydrated gold atoms to find out how their interactions depended on their separation. The two gold atoms were submerged in 31 explicit water molecules, equilibrated by classical molecular dynamics (MD) simulations, in which the oxygen atoms of 12 water molecules were fixed to ascertain that the golds were always surrounded by water. In the ab-initio calculations (optimization), the two gold atoms were fixed at different distances, 2.45 to 6.5 Å (6.95 Å – second system). At each step, we optimized the system before changing the Au-Au separation by 0.15 Å. All the systems were optimized by the Hartree-Fock method. H and O atoms were calculated in the 6-311+G* basis set and gold atoms were calculated with the LanL2DZ effective core potential basis set. Once these optimizations have converged, we performed single point energy calculation by the MP2 method with the same basis set. All these optimizations and single point energy calculations were performed by Gaussian09.[34]

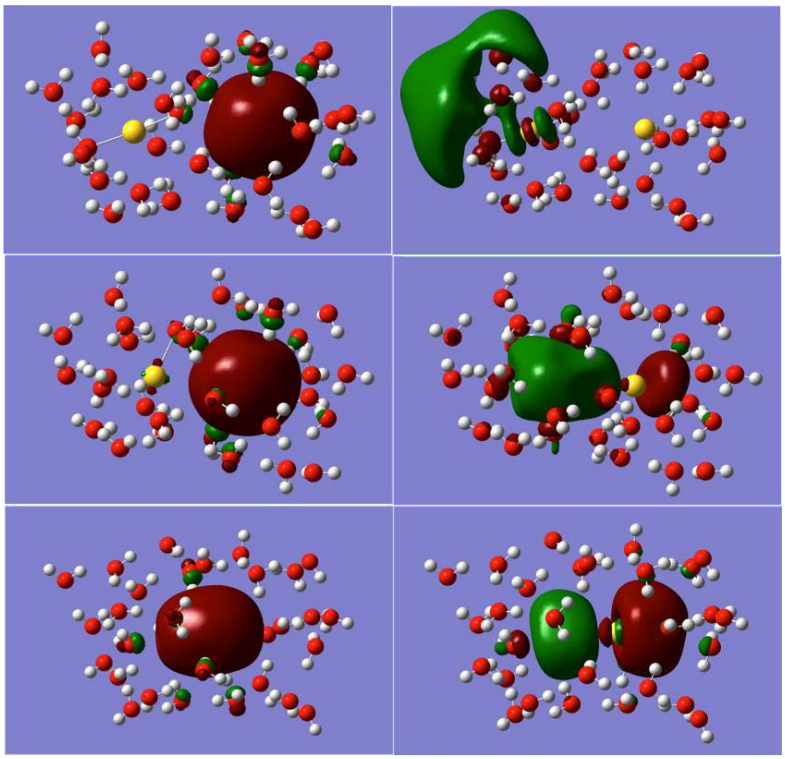

Supp. Fig. 24:
Bringing two hydrated gold atoms closer together.
(**Top**) 5.45 Å Au-Au separation, (**Middle**) 4.25 Å separation, (**Bottom**) 2.6 Å separation.

(**Left**) Highest Occupied Molecular Orbital (HOMO) of the system, (**Right**) Lowest Unoccupied Molecular Orbital (LUMO) of the system.

During the optimizations, the two gold atoms formed a cation-anion pair, when their separation was more than 5 Å (Figure 4 and Supp. Fig. 24). The cation was formed by a positively charged linear complex with two water molecules surrounding a gold atom ($[Au(H_2O)_2]^{+1}$), while the anion was formed by the second gold atom only. The partial charge of the cation complex was 0.7e to 0.8e whereas the charge of the anionic gold was about -1e, giving a hydration shell with 3-5 waters. The HOMO consisted of the valence orbital of the anionic gold atom and the LUMO was centered on the cationic gold complex (Supp. Fig. 24). When the gold separation decreased below 5 Å, both atoms started to contribute to HOMO and LUMO. At 4.25 Å, the gold atom in the cationic complex contributed very little in HOMO, but the anionic gold contributed significantly in LUMO (Supp. Fig. 24). As the gold-gold separation decreased, the linear cationic complex was gradually

turned into a positively charged gold atom coordinated to three waters. This type of water arrangement and charge distribution could be seen when the separation between two gold atoms was 4.55-3.5 Å. At even closer distances, the two gold atoms became gradually coordinated and discharged. When the Au-Au separation was reduced below 3.5 Å, the system again changed noticeably, since there was almost equal contribution of both gold atoms in HOMO and LUMO (Supp. Fig. 24). However, one gold atom was almost neutral and the charge of the other one was -0.5e to -0.6e. The neutral gold atom interacted with a single water molecule, which polarized the gold pair.

In Figure 4b of the main text, we plot the relative energy of the simulated system as a function of the separation between two gold atoms. The plot shows two minima, one (global) at 2.6 Å (1st) and the other (local) at 5.45 Å (2nd). The 1st minimum, which corresponds to the binding distance of the gold atoms, was by 31.8 kcal/mol more stable than the 2nd minimum, which is determined by the van der Waals attraction of the hydrated gold atoms and the existence of the cationic complex. There is a barrier of 7.65 kcal/mol associated with breaking of the cationic complex and reorganization of the whole system. The 2nd minimum corresponds to the metastable state accessed through the spinodal decomposition of gold atoms in water. The spinodal separation alone can be associated with large gold-gold coupling enthalpy, which can be matched by an entropic term at only low gold concentration. At the current solvated gold concentration the system thus demixes in two phases (enthalpy dominated: gold rich, entropy dominated: gold poor)

Supplementary Section 14. Qualitative molecular dynamics simulation of liquid-liquid phase demixing.

We performed approximate classical atomistic molecular dynamics (MD) simulations, with NAMD,[35] to validate the spinodal decomposition of free, **neutral** gold atoms (Au) in water. Here, the primary goal is to qualitatively show that strong dispersion forces between water and gold can cause a supersaturated aqueous gold solution to spontaneously demix into hydrated spinodal structures that resemble our observations (e.g. Figure 2a of main text). To make this qualitative demonstration computationally feasible, we accelerated the dynamics in our model by ignoring frustrated interaction in many-body interactions (Supplementary Section 13), but focused only on pair-wise interactions.

We prepared a TIP3P water box (150×150×150 Å^3) randomly distributed with 1016 gold atoms (0.5 M concentration). In these simulations, nonbonding interactions were calculated using a cut-off distance of d = 10 Å and long range electrostatic interactions were calculated by the PME method[36] in the presence of periodic boundary conditions. The system was simulated in the NPT ensemble at P = 1 atm using a Langevin dynamics with a damping constant of γ_{Lang} = 0.1 ps^{-1} and 2 fs time steps. In the simulation, we used the NBFIX facility[37] which overwrote potential well depths and the van der Waals radius on the standard rule with specific atom-pair Lennard-Jones parameters.

CHARMM forcefield[38] was used for the bond, and angle parameters of water and water-water nonbonding interactions. For Au-H interaction (gold with hydrogen of water), we used the Lennard-Jones interactions data between the gold (100) surface with hydrogen of the hydroxyl group using Wright *et al.*'s calculation.[39] The Au-Au and Au-O (oxygen of water) interactions in water solvent were estimated by performing MP2 level *ab-initio* calculations (implicit water solvent) using the 6-31G* basis set for H, O and LanL2DZ effective core potential basis set for Au. All *ab-initio* calculations were performed by Gaussian09.[34] We performed the single point energy calculations while changing the distance between the two gold atoms. The energy plot as a function of distance between the two gold atoms passed through a minimum at a gold-gold separation of 2.6 Å. Hence, we

used 2.6 Å as the radius for Au-Au interactions. We calculated the energy difference of 66 kcal/mol for the two-gold systems at Au-Au distances of 2.6 Å and 6 Å. This energy was set as the well depth in the Lennard-Jones like potential used for gold-gold coupling in the atomistic MD simulations.

To obtain the Au-O interaction parameters, we prepared a system with one gold atom and one water molecule in implicit water solvent. Similar to the Au-Au case, we first optimized the structure and then performed a distance-dependent study for Au and water. In the optimized structure the oxygen of water was directed towards the gold atom and the distance between the gold and oxygen was 2.52 Å. This value was then used as the effective radius in the Au-O interaction. From the distance-dependent calculations, we found the interaction strength of Au-water to be 43.6 kcal/mol, which was used as the well depth for the Au-O interaction.

The results of these (qualitative) MD simulations obtained with the above parameters are captured in Supp. Fig. 25, where an initially random collection of gold atoms in water spontaneously demixes into a composition that strongly resembles the spinodal structures in Figure 2a of the main text.

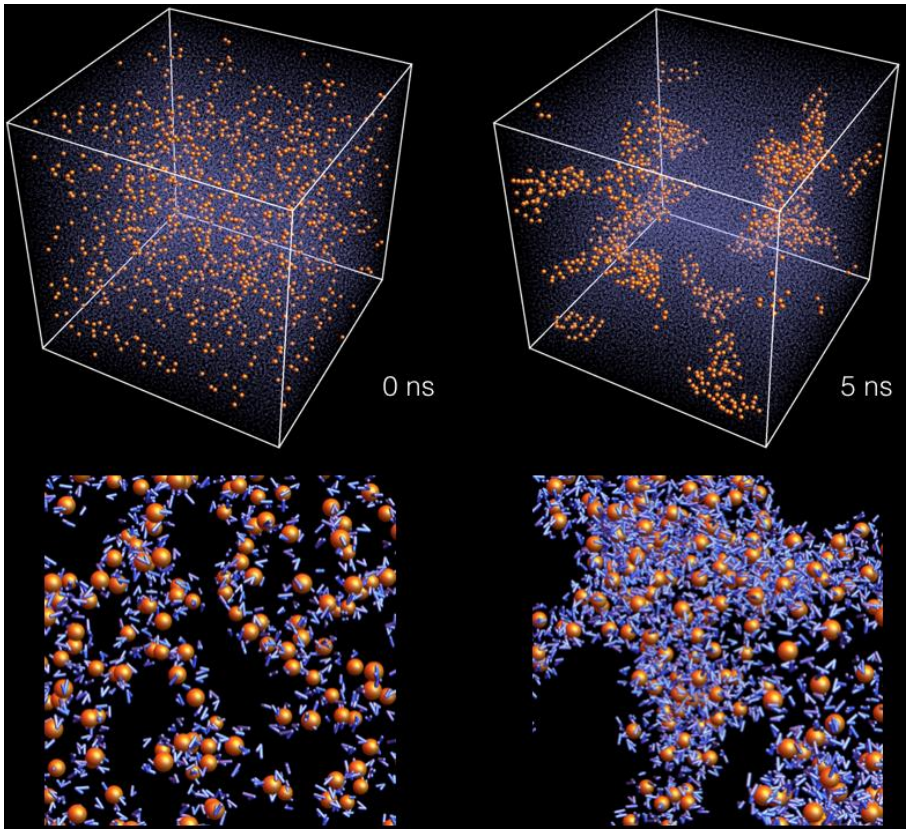

Supp. Fig. 25. Spontaneous demixing of Au^0 and water in qualitative molecular dynamics simulations. (**Top row**) A random distribution of 1016 zero-valent Au^0 atoms (orange spheres) interspersed with water molecules (light blue point cloud) within a 150 $Å^3$ volume (0.5 M concentration) spontaneously demixes into structurally amorphous gold-rich and gold-poor regions. (**Bottom row**) Identical viewpoints of magnified simulation snapshots in the top row show gold atoms (1.3 Å-radius spheres) and only their neighbouring water molecules (blue bent lines). Gold-rich aqueous phases start forming at t = 5 ns. Because many-body interactions are approximated here, the time scales in this simulation occur much faster than in a real system.

Supplementary Section 15. Preliminary results on multi-step nucleation in Ag-water system.

Radiolysis-induced nucleation also occurs in other noble-metal systems, such as silver [40]. Here, we present preliminary evidence of multi-step nucleation in aqueous silver nitrate.

Using the same TEM liquid cell setup described in Supplementary Section 1, 1 mM of $AgNO_3$ (Purity:99.999% Cat #: 204390 Sigma-Aldrich Co. LLC., St Louis, MO, USA) is allowed to nucleate under electron beam using a dose rate of 5200 e $Å^{-2}$ s^{-1}. A sequence of images captured from this experiment is shown in Supp. Fig. 26. The estimated initial concentrations of neutral Ag

The same multi-step nucleation for gold captured in Figures 1-2 (main text) and Supp. Figs. 9-10 appears for the silver nucleating in Supp. Fig. 26: (I) Ag-rich liquid regions (yellow arrows) form via spinodal decomposition, from which (II) amorphous Ag nanoclusters form, that finally (III) crystallize into FCC nanocrystals. Compared to Au nanoclusters, Ag nanoclusters have poorer contrast against solution because of the latter's much lower atomic number. Furthermore, fully reducing aqueous Ag(I) has a lower redox potential than aqueous Au(III),[40,41] which explains why nucleating Ag nanoclusters requires a higher electron dose rate than Au nanoclusters.

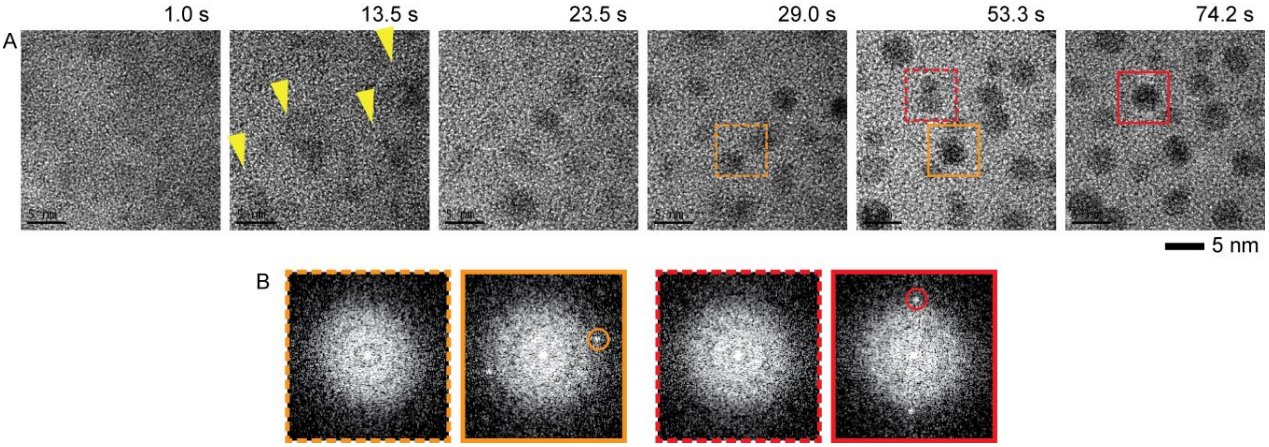

Supp. Fig. 26. Three-step pathway for silver (Ag) nucleation in water. (**A**) Raw TEM images and **(B)** low-pass filtered TEM images showing the intermediate steps in nucleating silver nanocrystals from a supersaturated aqueous Ag^0. From 1.0-13.5 s, supersaturated Ag^0 solution spontaneously demixes into Ag-poor and Ag-rich liquid phases (lighter and darker regions, respectively) *via* spinodal decomposition. The yellow arrows in (B) indicate Ag-rich liquid phases that collapse into Ag amorphous clusters, which then crystallize and show diffraction contrast. (**C**) Fourier transforms of cropped square regions (orange and red) in panels (A), with the Ag{111} FCC reciprocal lattice spacing circled in orange and red.

Supplementary References:

1. Zheng, H. *et al.* Observation of Single Colloidal Platinum Nanocrystal Growth Trajectories. *Science* **324,** 1309–1312 (2009).
2. Lu, J., Aabdin, Z., Loh, N. D., Bhattacharya, D. & Mirsaidov, U. Nanoparticle Dynamics in a Nanodroplet. *Nano Lett.* **14,** 2111–2115 (2014).
3. Seltzer, S. M. & Berger, M. J. Evaluation of the collision stopping power of elements and compounds for electrons and positrons. *Int. J. Appl. Radiat. Isot.* **33,** 1189–1218 (1982).
4. Buxton, G. V, Greenstock, C. L., Helman, W. P. & Ross, A. B. Critical review of rate constants for reactions of hydrated electrons, hydrogen atoms and hydroxyl radicals. *Phys. Chem. Ref. Data* **17,** 513–886 (1988).
5. Grogan, J. M., Schneider, N. M., Ross, F. M. & Bau, H. H. Bubble and Pattern Formation in Liquid Induced by an Electron Beam. *Nano Lett* **14,** 359–364 (2014).
6. Arakaki, T. & Faust, B. C. Sources, sinks, and mechanisms of hydroxyl radical (•OH) photoproduction and consumption in authentic acidic continental cloud waters from Whiteface Mountain, New York : The role of the Fe (r) (r = II , III) photochemical cycle phases of Civil En. *J. Geophys. Res.* **103,** 3487–3504 (1998).
7. Pimblott, S. M. & LaVerne, J. A. Molecular product formation in the electron radiolysis of water. *Radiat. Res.* **129,** 265–271 (1992).
8. Hart, E. J. The Hydrated Electron. *Science* **146,** 19–25 (1964).
9. Gachard, E. *et al.* Radiation-induced and chemical formation of gold clusters . *New J. Chem.* **22,** 1257–1265 (1998).
10. Mirsaidov, U. M., Zheng, H., Bhattacharya, D., Casana, Y. & Matsudaira, P. Direct observation of stick-slip movements of water nanodroplets induced by an electron beam. *Proc. Natl. Acad. Sci.* **109,** 7187–7190 (2012).
11. Jain, A. & Goodson, K. E. Measurement of the Thermal Conductivity and Heat Capacity of Freestanding Shape Memory Thin Films Using the 3ω Method. *J. Heat Transfer* **130,** 102402 (2008).
12. Belloni, J., Mostafavi, M., Remita, H., Marignier, J.-L. & Delcourt, and M.-O. Radiation-induced synthesis of mono- and multi-metallic clusters and nanocolloids. *New J. Chem.* **22,** 1239–1255 (1998).
13. Yao, T. *et al.* Insights into Initial Kinetic Nucleation of Gold Nanocrystals. *J. Am. Chem. Soc.* **132,** 7696–7701 (2010).
14. Reimer, L. & Kohl, H. *Transmission Electron Microscopy*. (Springer, New York, 2008).
15. Mayol, R. & Salvat, F. Total and Transport Cross Sections for Elastic Scattering of Electrons By Atoms. *At. Data Nucl. Data Tables* **65,** 55–154 (1997).
16. Israelachvili, J. N. *Intermolecular and Surface Forces*. (Academic Press, Cambridge, MA, 2011).
17. Butt, H.-J., Graf, K. & Kappl, M. *Physics and Chemistry of Surfaces*. (Wiley-VCH, Weinheim, 2013).
18. Wilson, A. J. C. The probability distribution of X-ray intensities. *Acta Crystallogr.* **2,** 318–321

(1949).

19. LaMer, V. & Dinegar, R. Theory, production and mechanism of formation of monodispersed hydrosols. *J. Am. Chem. Soc.* **72,** 4847–4854 (1950).

20. Robb, D. T. & Privman, V. Model of nanocrystal formation in solution by burst nucleation and diffusional growth. *Langmuir* **24,** 26–35 (2008).

21. Privman, V., Goia, D. V, Park, J. & Matijevic, E. Mechanism of Formation of Monodispersed Colloids by Aggregation of Nanosize Precursors. *J. Colloid Interface Sci.* **213,** 36–45 (1999).

22. Seidell, A. & Linke, W. F. *Solubilities of Inorganic and Metal-Organic Compounds*. (Van Nostrand, Princeton, NJ., 1958).

23. Kalikmanov, V. I. *Nucleation Theory, Lecture Notes in Physics*. (Springer, New York, 2013).

24. Guenther, G. & Guillon, O. Models of size-dependent nanoparticle melting tested on gold. *J. Mater. Sci.* **49,** 7915–7932 (2014).

25. Sambles, J. R. An Electron Microscope Study of Evaporating Gold Particles: The Kelvin Equation for Liquid Gold and the Lowering of the Melting Point of Solid Gold Particles. *Proc. R. Soc. A Math. Phys. Eng. Sci.* **324,** 339–351 (1971).

26. Buffat, P. & Borel, J. Size Effect on Melting Temperature of Gold Particles. *Phys. Rev. A* **13,** (1976).

27. Chushak, Y. G. & Bartell, L. S. Melting and Freezing of Gold Nanoclusters †. *J. Phys. Chem. B* **105,** 11605–11614 (2001).

28. Mendez-Villuendas, E. & Bowles, R. Surface Nucleation in the Freezing of Gold Nanoparticles. *Phys. Rev. Lett.* **98,** 185503 (2007).

29. Mendez-Villuendas, E. & Bowles, R. Erratum: Surface Nucleation in the Freezing of Gold Nanoparticles [Phys. Rev. Lett. 98, 185503 (2007)]. *Phys. Rev. Lett.* **99,** 159901 (2007).

30. Gránásy, L. Diffuse interface theory of nucleation. *J. Non. Cryst. Solids* **162,** 301–303 (1993).

31. Oono, Y. & Puri, S. Computationally efficient modeling of ordering of quenched phases. *Phys. Rev. Lett.* **58,** 836–839 (1987).

32. Mikhlin, Y. *et al.* Submicrometer intermediates in the citrate synthesis of gold nanoparticles: New insights into the nucleation and crystal growth mechanisms. *J. Colloid Interface Sci.* **362,** 330–336 (2011).

33. Vekilov, P. G. Dense Liquid Precursor for the Nucleation of Ordered Solid Phases from Solution. *Cryst. Growth Des.* **4,** 671–685 (2004).

34. Frisch, M. J. *et al.* Gaussian 09 Revision D.01. (2009).

35. Phillips, J. C. *et al.* Scalable molecular dynamics with NAMD. *J. Comput. Chem.* **26,** 1781–802 (2005).

36. Darden, T., York, D. & Pedersen, L. Particle mesh Ewald: An N · log(N) method for Ewald sums in large systems. *J. Chem. Phys.* **98,** 10089 (1993).

37. Baker, C. M., Lopes, P. E. M., Zhu, X., Roux, B. & Mackerell, A. D. Accurate Calculation of Hydration Free Energies using Pair-Specific Lennard-Jones Parameters in the CHARMM Drude Polarizable Force Field. *J. Chem. Theory Comput.* **6,** 1181–1198 (2010).

38. MacKerell, Jr., A. D. *et al.* All-atom empirical potential for molecular modeling and dynamics studies of proteins. *J. Phys. Chem. B* **5647,** 3586–3616 (1998).

39. Wright, L. B., Rodger, P. M., Corni, S. & Walsh, T. R. GolP-CHARMM: First-Principles Based Force Fields for the Interaction of Proteins with Au(111) and Au(100). *J. Chem. Theory Comput.* **9,** 1616–1630 (2013).

40. Belloni, J. Nucleation, growth and properties of nanoclusters studied by radiation chemistry: Application to catalysis. *Catal. today* **113,** 141–156 (2006).

41. Henglein, A. The Reactivity of Silver Atoms in Aqueous Solutions (A y-Radiolysis Study). *Berichte der Bunsengesellschaft für Phys. Chemie* **81,** 556–561 (1974).